The Astrophysical Journal, 971:24 (27pp), 2024 August 10 https://doi.org/10.3847/1538-4357/ad487d

A Multiwavelength Survey of Nearby M Dwarfs: Optical and Near-ultraviolet Flares and Activity with Contemporaneous TESS, Kepler/K2, Swift, and HST Observations

Rishi R. Paudel[1,2,3,4], Thomas Barclay[5], Allison Youngblood[5], Elisa V. Quintana[5], Joshua E. Schlieder[5], Laura D. Vega[1,3,16], Emily A. Gilbert[6], Rachel A. Osten[7], Sarah Peacock[4,5], Isaiah I. Tristan[8,9,10], Dax L. Feliz[11], Patricia T. Boyd[5], James R. A. Davenport[12], Daniel Huber[13], Adam F. Kowalski[8,9,10], Teresa Monsue[5,14], and Michele L. Silverstein[15,17]

[1] CRESST II and Exoplanets and Stellar Astrophysics Laboratory, NASA/GSFC, Greenbelt, MD 20771, USA; rishi.pkr061@gmail.com
[2] Southeastern Universities Research Association, 1201 New York Avenue NW, Suite 430, Washington, DC 20005, USA
[3] University of Maryland, College Park, MD 20742, USA
[4] University of Maryland, Baltimore County, Baltimore, MD 21250, USA
[5] NASA Goddard Space Flight Center, Greenbelt, MD 20771, USA
[6] NASA Jet Propulsion Laboratory, 4800 Oak Grove Drive, Pasadena, CA 91109, USA
[7] Space Telescope Science Institute, 3700 San Martin Drive, Baltimore, MD 21218, USA
[8] Department of Astrophysical and Planetary Sciences, University of Colorado Boulder, 2000 Colorado Avenue, Boulder, CO 80305, USA
[9] Laboratory for Atmospheric and Space Physics, University of Colorado Boulder, 3665 Discovery Drive, Boulder, CO 80303, USA
[10] National Solar Observatory, University of Colorado Boulder, 3665 Discovery Drive, Boulder, CO 80303, USA
[11] American Museum of Natural History, 200 Central Park West, New York, NY 10024, USA
[12] Department of Astronomy, University of Washington, Box 351580, Seattle, WA 98195, USA
[13] Institute for Astronomy, University of Hawai'i, 2680 Woodlawn Drive, Honolulu, HI 96822, USA
[14] Institute of Astrophysics & Computational Sciences, The Catholic University of America, 620 Michigan Avenue NE, Washington, DC 20064, USA
[15] US Naval Research Laboratory, 4555 Overlook Avenue SW, Washington, DC 20375, USA

Received 2024 February 4; revised 2024 April 3; accepted 2024 April 6; published 2024 August 1

Abstract

We present a comprehensive multiwavelength investigation into flares and activity in nearby M dwarf stars. We leverage the most extensive contemporaneous data set obtained through the Transiting Exoplanet Sky Survey, Kepler/K2, the Neil Gehrels Swift Observatory, and the Hubble Space Telescope, spanning the optical and near-ultraviolet (NUV) regimes. In total, we observed 213 NUV flares on 24 nearby M dwarfs, with ∼27% of them having detected optical counterparts, and found that all optical flares had NUV counterparts. We explore NUV/optical energy fractionation in M dwarf flares. Our findings reveal a slight decrease in the ratio of optical to NUV energies with increasing NUV energies, a trend in agreement with prior investigations on G–K stars' flares at higher energies. Our analysis yields an average NUV fraction of flaring time for M0–M3 dwarfs of 2.1%, while for M4–M6 dwarfs it is 5%. We present an empirical relationship between NUV and optical flare energies and compare to predictions from radiative hydrodynamic and blackbody models. We conducted a comparison of the flare frequency distribution (FFDs) of NUV and optical flares, revealing that the FFDs of both NUV and optical flares exhibit comparable slopes across all spectral subtypes. NUV flares on stars affect the atmospheric chemistry, the radiation environment, and the overall potential to sustain life on any exoplanets they host. We find that early and mid-M dwarfs (M0–M5) have the potential to generate NUV flares capable of initiating abiogenesis.

Unified Astronomy Thesaurus concepts: Stellar flares (1603); M dwarf stars (982); Near ultraviolet astronomy (1094); Optical astronomy (1776)

Supporting material: machine-readable tables

1. Introduction

M dwarfs, characterized by their low mass (M $\lesssim 0.6\ M_\odot$) and cool effective temperatures ($T_{\rm eff} \lesssim 4000$ K), represent the most abundant stellar objects, accounting for approximately 75% of the total stellar population within our Galaxy (Henry et al. 2006). The small radii of M dwarfs make them favorable hosts to several exceptional planetary systems that enable deep follow-up investigations via mass measurements and transmission and emission spectroscopy. These stars are the primary targets of ongoing planet-search missions like the Transiting Exoplanet Survey Satellite (TESS; Ricker et al. 2015) and the CHaracterising ExOPlanets Satellite (CHEOPS; Benz et al. 2021), and M dwarfs are more likely to host more Earth-sized planets, compared to higher-mass stars (Dressing & Charbonneau 2015; Hardegree-Ullman et al. 2019).

Stellar flares are transient events observed as photon emission across the electromagnetic spectrum, including gamma-rays, X-rays, UV, optical, infrared, and radio waves (Osten et al. 2005; Fuhrmeister et al. 2008). These events occur when the conversion of magnetic energy, previously stored in the magnetic field, to kinetic energy through magnetic reconnection leads to the acceleration of particles and the deposition of the particles' energy into the atmosphere through collisions with atmospheric molecules (e.g., heating). The spectral energy distributions of solar and stellar flares consist of emission lines and continuum.

---

[16] Heising-Simons Astrophysics Postdoctoral Launch Program Fellow.

[17] Resident guest investigator as a National Research Council (NRC) Research Associate.

Typically, the continuum emission observed across ultraviolet and optical wavelengths is characterized as a high-temperature blackbody (BB) with a temperature around 10^4 K (Hawley & Fisher 1992). However, this model has been shown to not accurately match all observations (Brasseur et al. 2023; Kowalski et al. 2019; Berger et al. 2023).

Though M dwarfs are cooler and less luminous than the Sun, they have relatively strong magnetic fields for their sizes. For example, WX UMa (an M5.5 dwarf) is reported to have average surface magnetic field $\langle B \rangle \approx 7.0$ kG (Shulyak et al. 2017), 70× that of the Sun (Solanki 2009). M dwarfs are capable of producing very strong flares with energies larger than that of the strongest flare observed on the Sun, irrespective of their ages (Günther et al. 2020; Schmidt et al. 2014; Hawley & Pettersen 1991; Paudel et al. 2018b, 2018a; France et al. 2020). In order to understand the potential influence of M dwarf flares on exoplanet atmospheres, it is important to characterize flare activity. This will, in turn, be helpful to estimate the energy received by planets in the form of X-ray and UV photons and energetic particles at different stages of stellar evolution and the cumulative effect of flares over the lifetime of a planet.

The near-ultraviolet (NUV) radiation (1700–3200 Å) of cool stars plays a crucial role in determining the habitability of terrestrial exoplanets. The NUV flux received by these planets can have both positive and negative impacts. On one hand, an excessive dose of NUV flux can be detrimental, as it has the potential to harm the DNA of surface organisms and dissociate key biosignature molecules like O_3 (Rugheimer et al. 2015a, 2015b). On the other hand, NUV photons within the 2000–2800 Å range are essential for prebiotic photochemistry, which contributes to the emergence of life (abiogenesis; Ranjan et al. 2020; Rimmer et al. 2018). Flares significantly enhance the NUV line and continuum emission flux by orders of magnitude (Kowalski et al. 2013; Brasseur et al. 2019; Chavali et al. 2022). In some cases, flares can provide the necessary NUV flux for abiogenesis when the quiescent NUV flux from the host star is insufficient. Therefore, flares play a vital role in determining the NUV conditions that impact exoplanetary atmospheres, biosignatures, and overall habitability.

Although numerous stellar flares have been observed by missions such as TESS and Kepler, only a limited number of flares have been simultaneously detected in both the optical and NUV wavelength bands. Consequently, the distribution of energy within flares across the optical and NUV wavelengths remains inadequately understood (Brasseur et al. 2023; Paudel et al. 2021). Most studies aiming to assess the impact of flares on exoplanets extrapolate findings from white-light flare investigations to the UV range (see, e.g., Feinstein et al. 2020b; Howard et al. 2020).

Various models are utilized to estimate the flare energies, and their complexity can vary. One approach assumes a single-temperature BB to estimate the bolometric energies of flares detected through single-bandpass photometry. For example, Shibayama et al. (2013) used a 9000 K BB model to estimate bolometric energies of flares detected with Kepler. On the other hand, alternative models combine these BB models with data derived from archived UV spectra, as demonstrated by Loyd et al. (2018). Nevertheless, the precision of UV predictions generated by these models has not been comprehensively tested. A study conducted by Kowalski et al. (2019) with the Hubble Space Telescope (HST) Cosmic Origins Spectrograph (COS) revealed that the 9000 K BB model underestimated both the NUV continuum and the overall NUV emission observed during two flares by a factor of 2–3. Furthermore, the peak flare temperatures can surpass temperatures of 9000 K (Kowalski et al. 2013; Howard et al. 2020). This introduces the need for greater complexity when constructing accurate flare models.

Brasseur et al. (2023) recently investigated the distribution of optical/NUV energy in stellar flares using overlapping data sets from the Galaxy Evolution Explorer (GALEX; Martin et al. 1999) and Kepler (Borucki et al. 2010). Their analysis primarily focused on G and K stars and identified 1557 NUV flares in GALEX light curves for which contemporaneous Kepler long-cadence (30 minute) data are available, as well as two NUV flares in GALEX light curves for which contemporaneous Kepler short-cadence (1 minute) data are available. Interestingly, none of the flares detected by GALEX were identified in the contemporaneous Kepler light curves. As a result, the authors established upper limits for flare energies in the Kepler band and for optical-to-NUV flare energy ratios.

The Brasseur et al. (2023) study revealed a correlation spanning approximately three orders of magnitude between the energy ratio of flares in the two bands and the energy in the GALEX NUV band (1693–3008 Å). They demonstrate that at lower flare energies the energy fractionation aligns with the predictions of some radiative hydrodynamic (RHD) models (Kowalski et al. 2017; Kowalski 2022). Such models were updated to incorporate both continuum and emission lines, thereby providing the flare's spectral energy distribution from NUV wavelengths to the optical range. However, for larger flares, mostly exceeding energies of 10^{33} erg, a significant deviation of up to approximately three orders of magnitude from the models was observed. The deviation appears as a disconnect between observed data and model predictions, but the underlying cause remains unclear.

Jackman et al. (2023) examined six empirical flare models to predict NUV and FUV flare rates in M dwarf stars based on white-light observations. Those models mainly consisted of a 9000 K BB spectrum, a modified BB spectrum with flux contributions from emission lines, a blend of 9000 K BB spectrum and UV spectra derived from the 1985 Great Flare of AD Leo (Hawley & Pettersen 1991), and a blend of 9000 K BB with NUV emission lines and an FUV flare model (Loyd et al. 2018). Jackman et al. (2023) used TESS data to determine average white-light flare rates for partially and fully convective M stars, supplementing this with GALEX data. They found that the 9000 K BB model underestimates the observed GALEX NUV flare energies of partially (M0–M2) and fully convective M dwarfs by up to a factor of 2.7 ± 0.6 and 6.5 ± 0.7, respectively. Furthermore, they found that the Loyd et al. (2018) flare model performs better than the other flare models considered but still underestimates the observed GALEX NUV flare energies of M dwarfs. It should be noted that the Loyd et al. (2018) flare model applies to inactive M dwarf flares and not to active stars like AD Leo.

In this paper, we study a sample of NUV flares observed on nearby M dwarfs of varying spectral types and ages by Swift and HST. We compare various NUV flare properties, such as flare durations, amplitudes, energies, and rates, with those of the optical flares using contemporaneous TESS and K2 data. We empirically determine the NUV/optical energy fractionation in M dwarf flares and compare with the predictive power of various RHD and BB flare models. This paper is organized as follows: Section 2 outlines the observation details, while Section 3 describes the analysis of both NUV and optical flares, as well as identification of NUV/optical flare counterparts. In Section 4 we interpret and discuss the results from this study, and in Section 5 we give a summary of the main results from this project.

2. Observation Overview

2.1. The Stellar Sample

Our sample of 34 M dwarfs was selected to cover a range of spectral subtype and ages in order to gather a more complete picture of M dwarf flaring activity. We selected from the brightest targets in three spectral subtype categories: early (M0–2.5), mid- (M3–5), and late (M5.5–7). Whenever possible, we included multiple stars of each category. Notably, our sample features some renowned flare stars and exoplanet host stars, including EV Lac, Proxima Centauri, AU Mic, and GJ 876 (e.g., Anglada-Escudé et al. 2016; Loyd et al. 2018; Plavchan et al. 2020; Paudel et al. 2021; Gilbert et al. 2022).

We present the details of the stellar sample in Table 1, including each star’s TESS Input Catalog (TIC) number, effective temperature ($T_{\rm eff}$), distance, spectral type (SpT), and age. Furthermore, we indicate whether the star is a planet host and/or part of a multiple system (MS), either binary or tertiary. Among the stars in our sample, nine are known to host one or more exoplanets, and an additional nine stars are known to have stellar companions.

Figure 1 shows the distribution of our sample stars in spectral type and age. For the stars that are assigned with a range of ages (see Table 1), the average values are used. Most of these ages were compiled from the literature. For some stars whose ages were not available in the literature, we estimated them using the period–age relation from Engle & Guinan (2023b). Stellar ages are notoriously difficult to estimate, and so caution should be exercised when using our age estimates. It is evident from Figure 1 that our M dwarf sample encompasses stars of various spectral types, ranging from M0 to M6.5, and spans a wide range of ages, from 22 Myr (AU Mic) to 11.5 Gyr (Kapteyn’s star). We do note that there are some gaps in age/spectral type space, due to the unavailability of bright stars in those parameter spaces.

2.2. TESS Data

The TESS (Ricker et al. 2015) mission, launched in 2018 April, was designed for a comprehensive photometric survey of the entire sky. It is equipped with four identical, red-sensitive, wide-field cameras, each of which enables surveillance of large portions of the sky in sectors spanning 24° × 96°. Each sector is observed continuously for ~27 days. While its primary objective is to detect small planets orbiting the nearest and brightest stars, it also exhibits sensitivity to low-amplitude, short-duration phenomena such as stellar flares. TESS’s photometric bandpass, spanning 600–1000 nm, is more sensitive to red objects like M dwarfs than the shorter-wavelength Kepler mission. TESS’s all-sky observational approach and its capacity to provide long-baseline and high-precision continuous time-series optical data make it particularly well suited for studying stellar flares (e.g., Günther et al. 2020; Gilbert et al. 2022; Howard & MacGregor 2022).

We acquired TESS data for our targets during Cycles 1 and 2 in its 2 minute cadence mode simultaneously with Swift as part of general investigator programs 1266 and 2252 (PI: J. Schlieder). The introduction of TESS 20 s cadence mode in Cycle 3 significantly advanced our ability to study the morphologies of white-light stellar flares. This mode allows for the detection of small flares that last for a few tens of seconds and may remain unnoticed in longer-cadence data or become entangled with other complex flares. We obtained simultaneous Swift and 20 s TESS data for six stars (AP Col, AU Mic, GJ 3631, Wolf 359, YZ Ceti, YZ CMi) during TESS Cycles 3 and 4 as part of general investigator programs 3273 (PI: L. Vega), 4247 (PI: L. Vega), and 4212 (PI: R. Paudel). Table 2 lists the TESS sectors, cadence utilized, and total observation time for each star. We used 20 s TESS data whenever they were available. For nine stars, either they were undetected in Swift's Ultra-Violet/Optical Telescope (UVOT) data or their UV data were not obtained in `EVENT` mode (which is necessary for extracting high-cadence light curves). Such stars are indicated by the footnote "a" next to their names in Table 1. In addition, TESS data are unavailable for one of the targets (WX UMa) in either 2 minute and 20 s cadence mode simultaneous with the Swift mission. We only have full-frame image (FFI) data obtained at 30 minute cadence for this target. Therefore, we only analyzed the TESS data of the remaining 24 stars.

We retrieved the light curves of our targets from the Mikulski Archive for Space Telescopes (MAST) using the `lightkurve` (Lightkurve Collaboration et al. 2018) package. We used the Pre-Search Data Conditioning (PDCSAP) light-curve products produced and made available by the TESS Science Processing Operations Center (SPOC; Jenkins et al. 2016). We specifically selected data points with quality flags 0 and 512. The latter flag, known as “impulsive outlier removed before cotrending,” often eliminates the peak of flares. However, to ensure that no flare data points were excluded, we included data with this quality flag as well. This approach helped minimize potential biases when estimating flare energies.

2.3. K2 Mission Data

One of our targets, Wolf 359, was observed simultaneously by the Kepler Space Telescope as part of the extended K2 mission (Howell et al. 2014) and Swift during Campaign 14 (2017 May 31–August 19) of the K2 mission as a part of general investigator program 14082 (PI: E. Quintana). The K2 data were obtained in both long-cadence (~30 minute; Jenkins et al. 2010) and short-cadence (~1 minute; Gilliland et al. 2010) mode for a total of ~80 days and are publicly available in MAST. We extracted the short-cadence light curve from the target pixel files using the methods explained in D. L. Feliz et al. (2024, in preparation).

2.4. Swift/UVOT Data

Thirty-three targets in our original sample were observed by Swift/UVOT (Roming et al. 2005) via Swift general investigator Cycle 14 program 1417229 (PI T. Barclay, Key Project “A Comprehensive, Multiwavelength Survey of Cool Star Activity”), as well as multiple additional programs through the mission’s Target of Opportunity (ToO) program. The remaining target, GJ 3631, was observed through joint TESS-

Table 1
Target List

Name	Other Name(s)	TIC	T_{mag} (mag)	Dist. (pc)	Ref.	T_{eff} (K)	SpT	Ref.	Planet Host	MS	Age	Ref.
AP Col	LP 949-15	160329609	9.66	8.66	(1)	2998	M4.5Ve	(1, 2)	...	...	40-50 Myr (Argus)	(2, 47)
AU Mic	HD 197481	441420236	6.76	9.72	(1)	3700	M1Ve	(3)	Yes (2)	...	24 $\pm$ 3 Myr (βPic)	(49)
AX Mic[a]	GJ 825	159746875	5.12	3.97	(1)	3729	M0V	(4)	...	...	4.8 Gyr	(39)
DG CVn	G 165-8	368129164	9.29	18.29	(5)	3175	M4Ve	(6)	...	Bin.	$\sim$20-200 Myr	(40)
DX Cnc	LHS 248	3664898	10.50	3.58	(1)	2814	M6.5V	(1, 7)	...	...	0.71 Gyr	(42)
EV Lac	GJ 873,LHS 3853	154101678	7.73	5.05	(1)	3270	M3.5e	(8)	...	...	125-800 Myr	(8)
EZ AQr[a]	GJ 866	402313808	8.30	3.40	(9)	3030	M5e	(10)	...	Tert.	0.87 Gyr	(42)
Fomalhaut C	LP 876-10	47423224	9.78	7.67	(1)	3132	M4V	(11)	...	Tert.	440 $\pm$ 40 Myr	(43)
GJ 1061[a]	LHS 1565	79611981	9.47	3.67	(1)	2905	M5.5V	(1, 12)	Yes (3)	...	>7.0 $\pm$ 0.5 Gyr	(44)
GJ 1284	HIP 116003	9210746	8.73	15.95	(1)	3406	M2Ve	(1, 13)	...	Bin.	110-800 Myr	(45)
GJ 205[a]	HD 36395	50726077	5.97	5.70	(1)	3700	M1.5	(14)	...	...	2.57 Gyr	(22)
GJ 3631	LHS 2320	281744438	11.7	13.9	(1)	3145	M5V	(37, 34)	...	...	0.72 Gyr	(42)
GJ 4353[a]	HIP 116645	224270730	9.80	20.71	(1)	3542	M2	(15)	...	...	0.89 Gyr	(42)
GJ 832	HIP 106440	139754153	6.68	4.96	(1)	3590	M2	(16)	Yes (2)	...	8.4 Gyr	(46)
GJ 1	HD 225213	120461526	6.67	4.35	(1)	3575	M1.5	(17)	...	...	5.7 Gyr	(42)
GJ 876	HIP 113020	188580272	7.58	4.68	(1)	3272	M4.0	(18)	Yes (4)	...	$8.4^{2.2}_{-2.0}$ Gyr	(48)
HIP 17695	G 80-21	333680372	9.32	16.79	(1)	3393	M4	(19)	...	...	149^{+51}_{-19} Myr (ABDor)	(49)
HIP 23309[a]	CD-57 1054	220473309	8.46	26.86	(1)	3886	M0	(19)	...	...	24 $\pm$ 3 Myr (βPic)	(49)
Kapteyn's star	HD 33793	200385493	7.05	3.93	(1)	3570	M1.5V	(20, 21)	Yes (2)	...	$11.5^{+0.5}_{-1.5}$ Gyr	(50)
Lacaille 9352	GJ 887, HD 217987	155315739	5.57	3.29	(1)	3676	M1V	(1, 22)	Yes (2)	...	2.9 Gyr	(22)
LHS 292[a]	GJ 3622	55099399	11.34	4.56	(1)	2784	M6.5	(17)	...	...	0.75 Gyr	(42)
LP 776-25	NLTT 14116	246897668	9.24	15.83	(1)	3414	M3.0V	(1, 23)	...	...	149^{+51}_{-19} Myr (ABDor)	(51, 49)
Luyten's star	GJ 273	318686860	7.31	5.92	(1)	3382	M3.5V	(24, 25)	Yes(4)	...	>8 Gyr	(52)
NLTT 31625[a]	L 471-3	144490040	9.75	28.35	(1, 26)	3594	M3	(27)	...	...	0.27 Gyr	(42)
Proxima Centauri	GJ 551	1019422535	7.58	1.30	(1)	3050	M5.5V	(28)	Yes (2)	...	4.85 Gyr	(41)
Ross 614	GJ 234 A	711366839	8.35	4.12	(1)	3154	M4.5Ve	(5, 29)	...	Bin.	0.76 Gyr	(42)
Twa 22	SSSPM J1017-5354	272349442	10.55	19.81	(1, 26)	3000	M5	(30)	...	Bin.	24 $\pm$ 3 Myr (βPic)	(54, 49)
UV Ceti[a]	GJ 65B	632499595	9.40	2.69	(1)	2728	M6.0	(31, 32)	...	Bin.	>0.5 Gyr	(53)
V1005 Ori	HIP 23200	452763353	8.43	24.38	(1)	3866	M0.5	(1, 33)	...	...	24 $\pm$ 3 Myr (βPic)	(55, 49)
Wolf 359	CN Leo, GJ 406	365006789	9.28	2.41	(1, 26)	2800	M6V	(34)	...	...	0.1-1.5 Gyr	(56)
Wolf 424	GJ 473	399087412	9.00	4.48	(1)	3013	M5.0	(17)	...	Bin.	0.70 Gyr	(42)
WX UMA[a]	LHS 39, GJ 412 B	252803606	10.71	4.90	(1)	2900	M5.5V	(34)	...	Bin.	3.0 Gyr	(22)
YZ Ceti	HIP 5643	610210976	12.30	3.72	(1)	3056	M4.5	(35)	Yes (3)	...	3.8 $\pm$ 0.5 Gyr	(42)
YZ CMi	GJ 285, HIP 37766	266744225	8.34	5.99	(1)	3100	M4.5e	(1, 36)	...	...	0.81 Gyr	(42)

Note. The column "MS" indicates whether the target is part of a multiple-star system.

[a] Indicates that either it was undetected in Swift/UVOT data or its Swift/UVOT data were not obtained in `EVENT` mode.

References. (1) Stassun et al. 2019; (2) Riedel et al. 2011; (3) Plavchan et al. 2020; (4) Debes et al. 2013; (5) Houdebine et al. 2019; (6) Mohanty & Basri 2003; (7) Stelzer et al. 2013; (8) Paudel et al. 2021; (9) Micela et al. 1997; (10) López-Valdivia et al. 2019; (11) Mamajek et al. 2013; (12) Henry et al. 2002; (13) Torres et al. 2006; (14) Rajpurohit et al. 2018; (15) Gaidos et al. 2014; (16) Houdebine et al. 2016; (17) Stelzer et al. 2013; (18) Stelzer et al. 2016; (19) Pineda et al. 2021; (20) Anglada-Escude et al. 2014; (21) Gizis 1997; (22) Mann et al. 2015; (23) Jeffers et al. 2018; (24) Boyajian et al. 2012; (25) Hawley et al. 1996; (26) Bailer-Jones et al. 2021; (27) Gaidos et al. 2014; (28) Anglada-Escudé et al. 2016; (29) Kirkpatrick et al. 1991; (30) Bonnefoy et al. 2014; (31) MacDonald et al. 2018; (32) Joy & Abt 1974; (33) Donati et al. 2008; (34) Cifuentes et al. 2020; (35) Astudillo-Defru et al. 2017b; (36) Baroch et al. 2020; (37) Sebastian et al. 2021; (38) Mamajek & Bell 2014; (39) Gáspár et al. 2013; (40) Riedel et al. 2014; (41) Kervella et al. 2003; (42) Engle & Guinan 2023a; (43) Mamajek 2012; (44) Dreizler et al. 2020; (45) Cardona Guillén et al. 2021; (46) Bryden et al. 2009; (47) Zuckerman 2019; (48) Veyette & Muirhead 2018; (49) Bell et al. 2015; (50) Guinan et al. 2016; (51) Bartlett et al. 2017; (52) Pozuelos et al. 2020; (53) Kervella et al. 2016; (54) Gagné et al. 2014; (55) Schlieder et al. 2012; (56) Bowens-Rubin et al. 2023.

(This table is available in machine-readable form.)

Table 2
Summary of TESS, Swift/XRT, and Swift/UVOT Observations

Name	TESS Sector	TESS Cadence	TESS Obs (days)	N_T	XRT Obs (ks)	UVOT Obs (ks)	$N_{\rm NUV}$
AP Col	6	2 minutes	20.6	65	36.0	36.6	10
	32	20 s	23.5	102	24.5	26.6	6
AU Mic	1	2 minutes	25.1	44	48.1	48.0	5
	27	20 s	22.6	71	20.8	17.2	1
DG CVn	23	2 minutes	18.7	96	24.5	25.5	3
DX Cnc	21	2 minutes	23.1	27	30.0	29.6	0
EV Lac	16	2 minutes	23.2	56	18.0	18.0	9
Fomalhaut C	2	2 minutes	25.0	62	42.1	32.8	8
GJ 1284	2	2 minutes	25.4	60	35.7	9.9	1
GJ 3631	46	20 s	22.2	82	85.4	86.1	16
GJ 832	1	2 minutes	25.4	0	39.0	38.7	0
GJ 1	2	2 minutes	25.4	0	29.5	29.2	0
GJ 876	2	2 minutes	25.4	0	38.1	37.9	0
HIP 17695	5	2 minutes	24.1	72	33.7	33.5	2
Kapteyn's star	4	2 minutes	20.5	0	35.1	34.9	0
Lacaille 9352	2	2 minutes	25.4	2	37.9	37.9	1
LP 776-25	5	2 minutes	24.1	75	34.8	30.6	3
Luyten's star	7	2 minutes	22.7	1	35.0	34.9	1
Prox. Cen.	11,12	2 minutes	47.7	134	82.9	64.9	20
Ross 614	6	2 minutes	20.4	60	34.7	34.0	22
TWA 22	9	2 minutes	22.7	78	37.1	37.3	6
V1005 Ori	5	2 minutes	24.0	35	32.6	34.2	4
Wolf 359	46	20 s	22.2	151	123.9	121.1	33
Wolf 424	23	2 minutes	18.1	63	13.0	12.9	5
YZ Ceti	3	2 minutes	17.9	63	36.6	36.5	11
	30	20 s	21.6	91	15.0	15.0	0
YZ CMi	7	2 minutes	22.7	123	37.1	37.0	21
	34	20 s	22.3	157	21.6	17.4	10

Note. N_T and $N_{\rm NUV}$ stand for the number of flares identified in the TESS and UVOT data, respectively.

(This table is available in machine-readable form.)

Swift observation program 4212 (PI: R. Paudel) during TESS Cycle 4. Almost all observations were performed with the UVM2 filter centered at $\lambda = 2259.8$ Å ($\lambda_{\rm min} = 1699.1$ Å, $\lambda_{\rm max} = 2964.3$ Å, FWHM = 527.1 Å). Few observations were performed with the UVW1 filter centered at $\lambda = 2629.4$ Å ($\lambda_{\rm min} = 1614.3$ Å, $\lambda_{\rm max} = 4730.0$ Å, FWHM = 656.6 Å). We did not observe any flares in the UVW1 filter except on Proxima Centauri. To enable the construction of high-cadence UV light curves and flexible binning, the observations were obtained in UVOT's EVENT mode. A summary of total observation times with Swift/UVOT for each target is listed in Table 2. We note that we did not acquire the Swift/UVOT data of six targets (AX Mic, EZ AQr, GJ 205, HIP 23309, UV Ceti, and NLTT 31625) in the `EVENT` mode.

Swift obtains simultaneous observations of each target using its X-ray Telescope (XRT; Burrows et al. 2005) alongside UVOT. Hence, all the targets in our sample were also observed by Swift/XRT via the same general investigator and ToO programs mentioned above. However, the primary goal of this paper is to compare optical and NUV flare properties and the activity of the targets. Therefore, we focus primarily on Swift NUV and data here. A detailed analysis of the X-ray flares observed on M dwarfs via this program and additional programs using the NICER X-ray telescope, as well as their comparison with contemporaneous TESS data, will be presented in a future publication. We present Swift/XRT observation time and the quiescent luminosity of each star in the XRT band in Tables 2 and 3, respectively.

2.4.1. Swift/UVOT Data Reduction

The raw data were obtained from the UK Swift Science Data Centre (UKSSDC) and then processed in two steps to obtain a cleaned event list. First, we used the `COORDINATOR`[18] FTOOL to convert raw coordinates to detector and sky coordinates. Second, we used `UVOTSCREEN` to filter the hot pixels and obtain a cleaned event list.

We utilized the FTOOL `UVOTEVTLC` task to extract calibrated light curves from the cleaned event lists. For the sources, we followed the recommended approach of employing a circular extraction region with a radius of 5″ centered around each source position except for some sources for which we used a radius of 7″. Such sources did not have a bright center and were somewhat elongated. Additionally, for a smooth background, we used a circular extraction region with a radius of 30″ located away from each source. We used `timebinalg=u` (uniform time binning) to create UVOT light curves with bins of 11.033 s. It is essential that the bin size is a multiple of the minimum time resolution of UVOT data, which is 11.033 ms. When photon pileup occurs on detectors, `UVOTEVTLC` incorporates a coincidence loss correction by utilizing the necessary parameters from CALDB. Subsequently, the light curves were corrected for barycentering using `BARYCORR`. To synchronize all the telescopes on a unified time system, the barycentric times were converted to the Modified Julian Date (MJD) system.

---

[18] https://heasarc.nasa.gov/ftools/caldb/help/coordinator.html

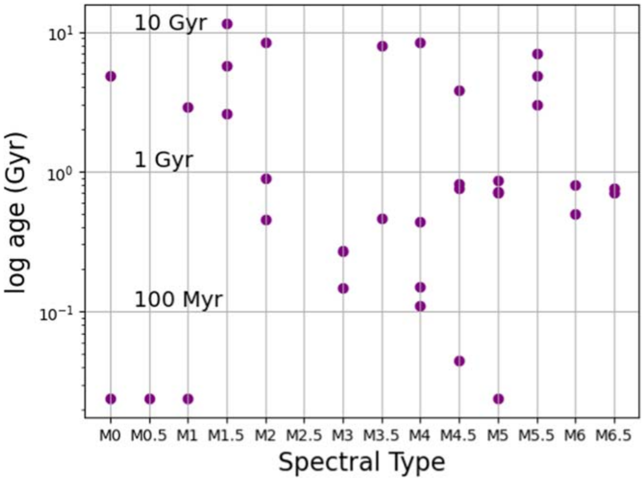

Figure 1. Distribution of M dwarfs in our sample by spectral type and age. The total number of M dwarfs is 34. We do not show error bars on the stellar ages, but we do note that in many cases they are imprecise.

We converted the count rate in each filter (UVM2 and UVW1) to flux density in units of erg cm^{-2} s^{-1} Å^{-1} by using an average count-rate-to-flux-density conversion ratio of 8.446×10^{-16} for the UVM2 filter and 4.209×10^{-16} for the UVW1 filter. The conversion ratio is part of the Swift/UVOT CALDB and was obtained using GRB models.[19] We estimated the quiescent NUV fluxes of each star by using these conversion ratios and the FWHM ($\Delta_{\rm uv}$ = 530 Å (UVM2) and $\Delta_{\rm uv}$ = 660 Å (UVW1)) of each filter. We list the quiescent NUV fluxes of the stars in Table 3. We note that three stars (GJ 1061, GJ 4353, and LHS 292) were undetected in Swift/UVOT data.

2.5. HST/STIS Data

We obtained time-series HST NUV spectra simultaneously with TESS for two targets, GJ 832 and GJ 1061, through general observer program 15463 (PI: A. Youngblood). All data were obtained with the STIS instrument's photon-counting NUV-MAMA detector with the G230L grating and 52″ × 2″ aperture. The time-series spectral data products cover wavelengths 1570−3180 Å at resolving power $R \sim 500$. GJ 832 was observed simultaneously with TESS Sector 1 for five consecutive orbits on 2018 August 15 from 15:52:07 to 22:47:13 for a total exposure time of 12,246 s. GJ 1061 was observed simultaneously with TESS Sector 3 for one orbit (one orbit lost owing to guide star acquisition error) on 2018 September 25 23:39:13 to 2018 September 26 00:23:55. Three consecutive orbits (one orbit lost owing to guide star acquisition error) were also obtained on 2019 February 21 10:43:44−14:34:06 for a total exposure time of 11,054 s; these three orbits were not performed simultaneously with TESS. The data were calibrated with the default CALSTIS v3.4.2 pipeline. We used the `stistools` Python package's `inttag` function to extract time-series spectra at a cadence of 10 s.

Table 3
Quiescent X-Ray and NUV Luminosities of Targets in Our Sample

Name	log L_X (erg s^{-1})	log $L_{\rm NUV}$ (erg s^{-1})	log $L'_{\rm NUV}$ (erg s^{-1})
AP Col	0.17	27.45	27.45
AU Mic	1.6	28.75	28.75
DG CVn	0.19	28.40	28.40
DX Cnc	0.035	27.10	27.10
EV Lac	1.0	27.90	27.90
Fomalhaut C	0.10	27.00	27.0
GJ 1284	0.29	28.30	28.30
GJ 3631	0.057	26.90	26.90
GJ 832	0.02	26.90	26.88
GJ 1	0.0098	26.70	26.68
GJ 876	0.0096	26.30	26.29
HIP 17695	0.21	28.30	28.30
Kapteyn's star	0.0077	26.50	26.48
Lacaille 9352	0.03	27.30	27.29
LP 776-25	0.25	28.20	28.20
Luyten's star	0.0051	26.50	26.49
Prox. Cen.		26.0	26.0
Ross 614	0.32	27.10	27.10
TWa 22	0.10	27.80	27.80
V1005 Ori	0.38	29.0	29.0
Wolf 359	0.13	26.10	26.10
Wolf 424	0.22	27.10	27.10
YZ Ceti	0.10	26.20	26.20
YZ CMi	0.58	27.90	27.90

Note. $L'_{\rm NUV}$ is the excess NUV luminosity.

(This table is available in machine-readable form.)

3. Flare Analysis

3.1. White-light Flares

3.1.1. Flare Identification

We used the `stella` package (Feinstein et al. 2020a) to identify flares in the TESS light curve. It employs convolutional neural networks (CNNs) and utilizes the flare catalog presented in Günther et al. (2020) to generate the required training, validation, and test sets for the CNNs. By utilizing `stella`, we obtained an initial estimate of the flare's location in the light curve and a corresponding "probability" value indicating the likelihood that each data point belongs to a flare. We considered data points with a probability greater than 0.5 and at least one directly adjacent flaring point as potential flare candidates. We further applied an additional criterion to each identified flare candidate. Specifically, the amplitude of the flare must exceed 2.5 times the standard deviation (σ) of the quiescent level. This criterion is often used in other flare studies such as Paudel et al. (2018a) and Brasseur et al. (2019). We list the number of optical flares identified in TESS light curves for each target in Table 2 in column N_T. We identified hundreds of flares in the K2 light curve of Wolf 359, the details of which will be provided in D. L. Feliz et al. (in preparation). Additionally, see Lin et al. (2021) for an analysis of the K2 light curve of Wolf 359.

Subsequently, we determined the stellar rotation periods by excluding all potential flare events, focusing solely on the quiescent light curve, and employing the Lomb−Scargle periodogram. As we utilized single TESS sector data for most of our targets, this approach is applicable only to stars that exhibit photometric spot variability in the TESS light curve

---

[19] https://heasarc.gsfc.nasa.gov/docs/heasarc/caldb/swift/docs/uvot/uvot_caldb_counttofluxratio_10wa.pdf

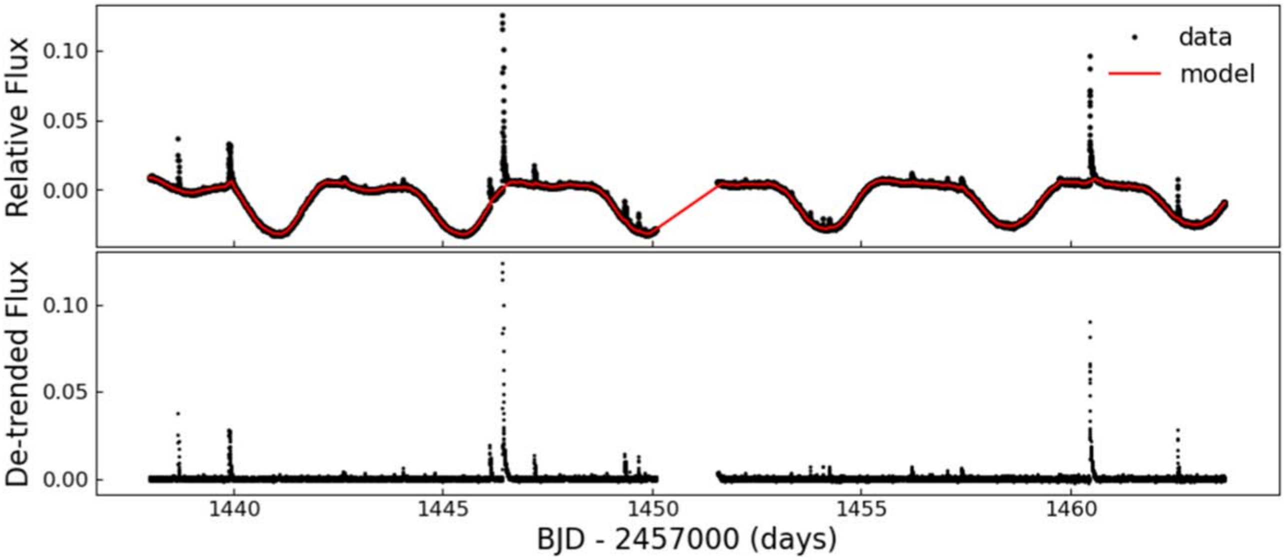

Figure 2. TESS light curve of V1005 Ori, obtained during Sector 5 (2018 November 15−December 11). The top panel shows the original light curve (black) and GP fit of the spot modulation (red). The rotation period of this star is 4.379 ± 0.337 days. The bottom panel displays the detrended light curve after subtracting the original quiescent light curve with rotational modulation.

Table 4
Rotation Periods, Bolometric Flare Luminosity ($L_{\mathrm{bol,flare}}$) Assuming a 10,000 K BB, and Radii of Targets

Name	Period (days)	P_{err} (days)	Reference	$L_{\mathrm{bol,flare}}$ (10^{30} erg s^{-1})	Radius ($R_{\odot}$)	Reference
AP Col	1.016	0.020	this work	7.57	0.29	(14)
AU Mic	4.872	0.361	this work	161	0.75	(15)
DG CVn	0.268	0.001	this work	20.2	0.46	(16)
DX Cnc	0.459	0.003	this work	0.88	0.12	(14)
EV Lac	4.319	0.337	this work	18.6	0.35	(17)
Fomalhaut C	0.318	0.002	this work	6.16	0.23	(14)
GJ 1284	7.335	0.946	this work, 1	57.4	0.56	(18)
GJ 3631	0.6920	0.0077	this work	4.31	0.19	(14)
GJ 832	55	…	2	…	…	…
GJ 1	60.1	5.7	5	…	…	…
GJ 876	96.7	…	6	…	…	…
HIP 17695	3.860	0.2452	this work	45.6	0.50	(19)
Kapteyn’s star	124.71	0.19	7	…	…	…
Lacaille 9352	∼200	…	8	61.6	0.47	(20)
LP 776-25	1.3708	0.031	this work	38.2	0.45	(14)
Luyten’s star	99	…	2	15.4	0.29	(3)
Prox. Cen.	82.600	0.100	10	1.98	0.14	(4)
Ross 614	1.585	0.049	this work	9.23	0.26	(14)
TWa 22	0.732	0.009	this work	15.3	0.41	(18)
V1005 Ori	4.379	0.337	this work	142	0.63	(9)
Wolf 359	2.72	0.04	Lin et al. 2021	1.16	0.14	(14)
Wolf 424	0.2073	0.001	this work	2.09	0.15	(9)
YZ Ceti	67	0.8	11	2.85	0.17	(12)
YZ CMi	2.774	0.133	this work	15.0	0.37	(13)

References. (1) Cardona Guillén et al. 2021; (2) Astudillo-Defru et al. 2017a; (3) Newton et al. 2015; (4) Boyajian et al. 2012; (5) Suárez Mascareño et al. 2015; (6) Correia et al. 2010; (7) Bortle et al. 2021; (8) Jeffers et al. 2020; (9) Houdebine et al. 2019; (10) Collins et al. 2017; (11) Engle & Guinan 2017; (12) Mann et al. 2015; (13) Baroch et al. 2020; (14) Sebastian et al. 2021; (15) Plavchan et al. 2020; (16) Osten et al. 2016; (17) Paudel et al. 2021; (18) Paegert et al. 2021; (19) Pineda et al. 2021; (20) Jeffers et al. 2020; (21) Newton et al. 2015; (22) Boyajian et al. 2012; (23) Houdebine et al. 2019; (24) Mann et al. 2015; (25) Baroch et al. 2020; (26) Lin et al. 2021; (27) this work.

(This table is available in machine-readable form.)

and stars with rotation periods less than 15 days. For all other stars, we gathered the rotation period values from existing literature. The rotation periods, which range from 0.2073 to 200 days, are provided in Table 4. For the periods we estimated, we also calculated uncertainties based on the half-width at half-maximum (HWHM) of the periodogram peaks, following the methodology suggested by Mighell & Plavchan (2013).

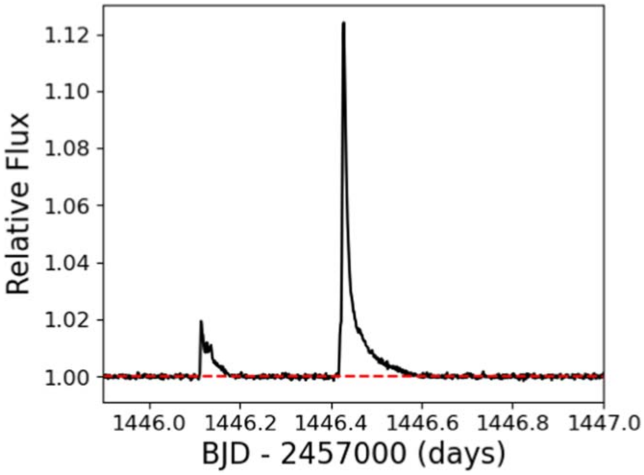

Figure 3. Example of flares identified in the TESS light curve of V1005 Ori shown in Figure 2. The red dashed line represents the quiescent level of the detrended light curve. The flux is normalized by the quiescent level flux.

The light curves were then detrended using the rotation period. To accomplish this, we used a periodic Gaussian process (GP) to model the starspot-modulated stellar rotation on the quiescent light curve using a "Rotation term" from `celerite` (Foreman-Mackey et al. 2017). The flux predicted by the model was subtracted from the total flux, resulting in the detrended light curve. Figure 2 demonstrates this procedure for one of our targets, V1005 Ori. Likewise, Figure 3 demonstrates two flares identified in the TESS light curve of V1005 Ori shown in Figure 2.

3.1.2. Determining Flare Properties

To determine the energies of the white-light flares, we first estimated the equivalent duration (ED) for each individual flare. The ED represents the duration over which a flare emits the same amount of energy as the star does during its quiescent state (Gershberg 1972). It is measured in units of time and depends on the filter used but is independent of the distance to the flaring object and is therefore widely used for determining flare energies. The ED of a flare is expressed as

$$\mathrm{ED} = \int \frac{\Delta F}{F_q} dt = \int \frac{F_f - F_q}{F_q} dt, \tag{1}$$

where F_f is the flaring flux and F_q is the quiescent flux of the star. We utilized the detrended light curves of the targets to estimate the EDs of the flares identified.

We can convert ED to absolute flare energy by using each star's spectral information whenever available (e.g., Paudel et al. 2021; Gilbert et al. 2022). However, we do not have homogeneous spectra for all the targets. Instead, we adopted the approach of Shibayama et al. (2013), which assumes a BB for the spectral energy distribution of each flare and estimates its energy using

$$E_{\mathrm{flare,bol}} = L_{\mathrm{flare}} \times \mathrm{ED}, \tag{2}$$

where

$$\begin{aligned} L_{\mathrm{flare}} &= \sigma T_{\mathrm{flare}}^4 A_{\mathrm{flare}} \\ &= \sigma T_{\mathrm{flare}}^4 \times \pi R_\star^2 \times \frac{\int B(T_{\mathrm{flare}}, \lambda) S(\lambda) d\lambda}{\int B(T_{\mathrm{eff}}, \lambda) S(\lambda) d\lambda}. \end{aligned} \tag{3}$$

In Equation (3), A_{flare} is the area of flare-emitting region, and L_{flare} is the bolometric luminosity of the flare and gives the energy emitted by a flare corresponding to ED of 1 s on a given star. Likewise, σ is the Stefan–Boltzmann constant, T_{flare} is the flare BB temperature, $R_\star$ and T_{eff} are the radius and effective temperature of a given star, respectively, $B(T, \lambda)$ is the Plank function, and $S(\lambda)$ is the spectral response function of the TESS instrument. We list the values of L_{flare} for a 10,000 K BB and $R_\star$ for each star in Table 4. Those values are listed for only those stars on which we observed flares with TESS.

Note that the value of L_{flare} depends on the assumed BB temperature. A 9000 K BB flare has 0.84× as much energy as a 10,000 K BB flare. A total of 21% of a 9000 K BB flare's bolometric energy is emitted in the TESS band, and likewise 18% for a 10,000 K BB. Similar estimates were obtained by previous studies, such as those by Maehara et al. (2021) and Schmitt et al. (2019).

3.2. NUV Flares

3.2.1. Swift/UVOT

The Swift/UVOT observations of any given target are broken into segments of 20–30 minutes owing to observing constraints of the mission. Because of this complexity and the short-duration observation of each target, we examined each light curve by eye to identify the flare candidates. Any event with two consecutive data points above the local noise level was identified as a flare. This noise level is different for each Swift/UVOT observing window. From here onward, any flare in the Swift/UVOT light curve will be referred to as an "NUV flare." We identified a total of 213 NUV flares, among which 199 (93.4%) were observed for their full duration. Furthermore, 15 NUV flares were observed on Wolf 359 by Swift/UVOT simultaneously with K2.

To compute the flare energies, we first estimated the ED of each flare in a similar manner to that done for the TESS flares. The flare energies E_{NUV} were computed by using the equation

$$E_{\mathrm{NUV}} = \mathrm{ED} \times 4\pi d_\star^2 \times F_q, \tag{4}$$

where $d_\star$ is the distance to the star and F_q is the quiescent flux in units of erg cm^{-2} s^{-1}. We list the properties of all the NUV flares in Appendix A.

Taking into account the small sample of NUV flares, we divide our targets into only two spectral bins, M0–M3 and M4–M6, which also approximately corresponds to partially convective and fully convective M dwarfs. In addition, we also divided the observed flare energies into four energy bins: 10^{27}–10^{29} erg, 10^{29}–10^{31} erg, 10^{31}–10^{33} erg, and $>10^{33}$ erg. We list the number of optical and NUV flares observed in each spectral and energy bin in Table 5. We find that the highest number of NUV flares is observed in the energy bin 10^{29}–10^{31} erg for both spectral bins. Likewise, we find that spectral bin M0–M3 has highest number of optical flares in the energy bin 10^{31}–10^{33} erg and M4–M6 has highest number of optical

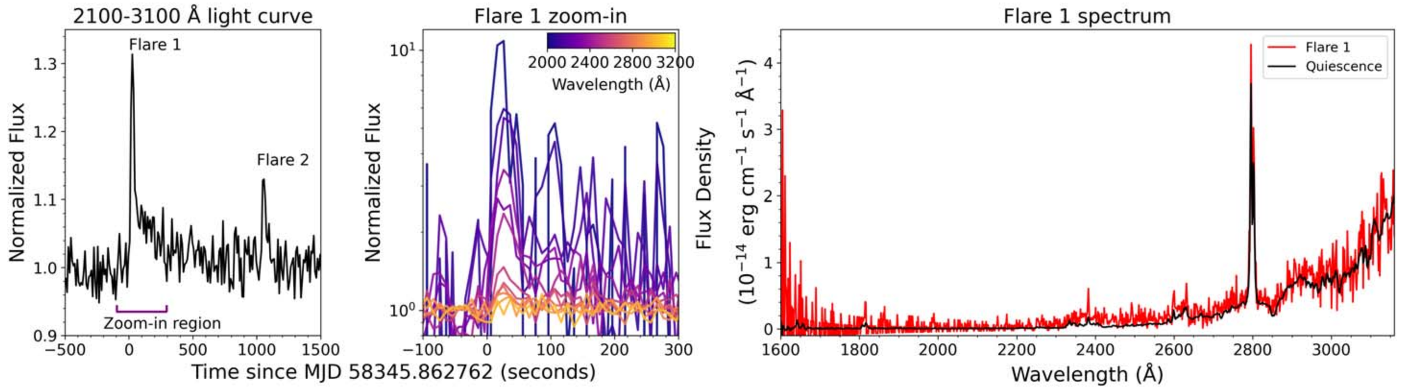

Figure 4. HST/STIS observations of GJ 832. Left: the 2100−3100 Å light curve at 10 s cadence normalized to the star's quiescent flux shown covers the 2000 s period when two flares, labeled Flare 1 and Flare 2, occurred. The purple horizontal bar shows the time period corresponding to the middle panel. Middle: a zoom-in of the 400 s period around Flare 1. A total of 12 light curves are shown, each corresponding to a 100 Å wide spectral bin from 2000 to 3200 Å. Note that the vertical axis is logarithmic to better visualize the wide range of flux enhancements seen over the STIS bandpass. Right: the average quiescent stellar spectrum (black) is compared to the stellar spectrum during a 27 s time period encompassing the brightest part of Flare 1 (red).

Table 5
Number of NUV/Optical Flares in Each Spectral and Energy Bin

Sp. Type	$10^{27}-10^{29}$ erg		$10^{29}-10^{31}$ erg		$10^{31}-10^{33}$ erg		$>10^{33}$ erg		Overall	
	$N_{\rm NUV}$	$N_{\rm optical}$	$N_{\rm NUV}$	$N_{\rm optical}$	$N_{\rm NUV}$	$N_{\rm optical}$	$N_{\rm NUV}$	$N_{\rm optical}$	$N_{\rm NUV}$	$N_{\rm optical}$
M0−M3	1	0	18	85	6	250	0	9	25	344
M4−M6	78	79	106	858	4	287	0	3	188	1227
Number of NUV Flares with Optical Counterparts										
M0−M3	0		4		3		0		7	
M4−M6	14		26		4		0		44	

Note. The fifth and sixth rows provide information regarding the number of NUV flares that had optical counterparts in a given energy bin.

flares in the energy bin $10^{29}-10^{31}$ erg. We did not observe any NUV flares with energies $>10^{33}$ erg.

3.2.2. HST/STIS

We observed GJ 832 and GJ 1061 with HST for five and four orbits, respectively. Like the Swift observations, the HST/STIS observations are also broken into segments of 30−45 minutes. Examining the light curves by eye, we identified two flares from GJ 832 (both occurred in the fourth orbit; obsid: odsx01020) and no flares in the GJ 1061 data. Figure 4 shows the two GJ 832 flare light curves and the spectrum of GJ 832 during quiescence and at the peak of the first flare. We computed a mean quiescent spectrum by averaging all five orbits. Note that the extremely short duration of the flares means that they have a negligible impact on the cumulative spectrum. We extracted flare spectra from obsid odsx01020 using the `inttag` and `x1d` functions with a start time of 988 s and a duration of 27 s for the first flare and a start time of 2019 s and a duration of 23 s for the second flare. Focusing on the 2100−3100 Å bandpass (i.e., ignoring the noisiest regions of the STIS spectrum), we determine that the first flare reached a peak relative amplitude 1.31× and the second flare reached 1.12×. The sharp rise and decay of each flare lasted approximately 60 and 40 s, respectively. The first flare exhibits an extended decay phase of over 10 minutes, and then the second flare occurred soon after. Simultaneous 2 minute TESS data show no evidence of either flare. We measure the two flares' EDs in the 2100−3100 Å bandpass to be 22.4 and 5.6 s. We calculate the flare energies following Equation (4) and find $\log_{10} E_f = 29.3$ and 28.7 erg. Note that the 2100−3100 Å wavelength range of this calculation is slightly different from the nominal UVM2 bandpass (1700−2960 Å).

3.3. Identifying White-Light/ NUV Flare Counterparts

To identify the optical counterparts to NUV flares, we visually examined the TESS/K2 and Swift/UVOT light curves after synchronizing the observation times of TESS/K2 and Swift/UVOT on a unified time system. Among the 213 detected NUV flares, we identified a sample of 51 flares that have optical counterparts. Out of those 51 NUV flares, 45 were observed for the full duration by Swift/UVOT. Furthermore, among the 213 NUV flares, 23 did not have simultaneous TESS data. When these flares occurred, either the corresponding stars were outside of TESS's field of view or TESS was downlinking data and not observing. Therefore, we found that ∼27% of NUV flares have optical counterparts.

The details of all NUV flares that have optical counterparts can be found in Appendix A, and those of corresponding optical counterparts can be found in Appendix B. In Appendix A, the NUV flares observed for their full duration and having detected optical counterparts are indicated by the footnote "a" in the third column labeled $N_{\rm U}$, while those not observed for their full duration but still having optical counterparts are indicated by the footnote "b." Likewise, footnote "c" signifies that simultaneous TESS/K2 data were unavailable for a given NUV flare.

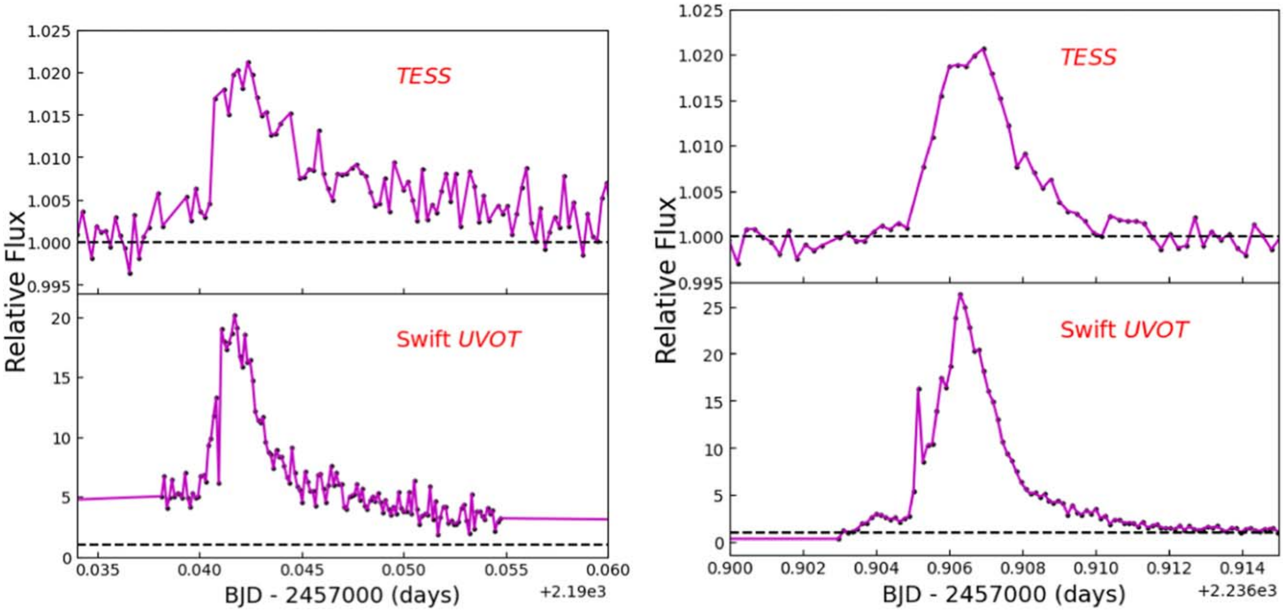

Figure 5. Flares observed simultaneously with both TESS and Swift/UVOT on two of our targets, AP Col (left panel) and YZ CMi (right panel), during TESS Sectors 32 and 34, respectively. Both stars were observed by TESS in 20 s cadence mode, and the displayed cadence of the Swift/UVOT data is ∼10 s. The black dashed line represents the quiescent level of each star in the corresponding band. The duration of the optical flare observed on AP Col is comparable to that of its NUV counterpart. Based on the optical counterpart, we can confirm that Swift/UVOT observed the NUV flare on AP Col for almost the entire duration, missing only a small portion of both the rise and decay phases. On the other hand, the duration of the NUV flare observed on YZ CMi is greater than its optical counterpart. The optical flares have peak fluxes ∼2% above the quiescent level, and the NUV flares have peak fluxes a factor of ∼20−25 above quiescence.

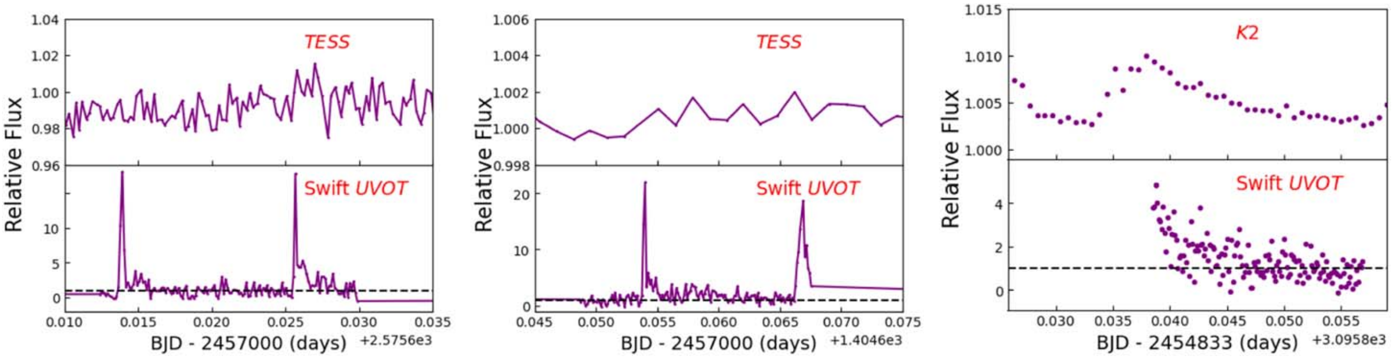

Figure 6. Left panel: NUV flares (bottom) undetected in the TESS 20 s light curve of GJ 3631 (top). Middle panel: NUV flares (bottom) undetected in the TESS 2 minute light curve of YZ Ceti (top). Right panel: elevation in the NUV flux of Wolf 359 (bottom) during a flare in the K2 1 minute light curve (top). The horizontal dashed line in each bottom panel represents the NUV quiescent level of a given star.

In Figure 5, we present two large flares that were observed simultaneously with both TESS and Swift/UVOT on two of our targets: AP Col (left panel) and YZ CMi (right panel).

The total number of NUV flares that have simultaneous TESS data but do not have optical counterparts is 135, among which 8 were not observed for the full duration by Swift/UVOT. Hence, we establish an upper limit on the optical flare energies for the remaining 127 NUV flares. We identified the TESS cadences closest to the NUV flare start times using the criterion that the maximum difference between the closest TESS cadence and the start time of a given NUV flare is less than the size of a single TESS cadence (i.e., 20 s or 120 s). We then calculated the maximum ED for the flare. The ED is the product of the maximum (flare) flux above quiescence at those TESS cadences (oftentimes a single TESS cadence for short-duration NUV flares) and the duration of a TESS cadence (20 s or 120 s). The maximum (flare) flux above the quiescent level is the difference of the quiescent flux and the sum of the observed flux and its corresponding uncertainty. The EDs were then calibrated to flare energies using bolometric flare luminosities listed in Table 4. There are 11 cases for which the maximum flux in the TESS light curve is slightly below the quiescent level, which makes the ED negative. We did not take into account such cases for further analysis of energy fractionation.

We demonstrate four NUV flares for which no optical counterparts were identified in the 20 s and 2 minute TESS light curves in the left and middle panels of Figure 6. From the two panels, we see that the flares are undetected because they are either diluted by the noise in the high-cadence light curve or suppressed owing to a longer cadence size.

We list the number of NUV flares for which optical counterparts were identified in TESS/K2 light curves for each spectral bin and energy bin mentioned above in Table 5. We find that 0%, 22.2%, and 50% of NUV flares observed on M0−M3 dwarfs had optical counterparts in the energy bins $10^{27}-10^{29}$ erg, $10^{29}-10^{31}$ erg, and $10^{31}-10^{33}$ erg, respectively. Likewise, 18%, 24.5%, and 100% of the NUV flares

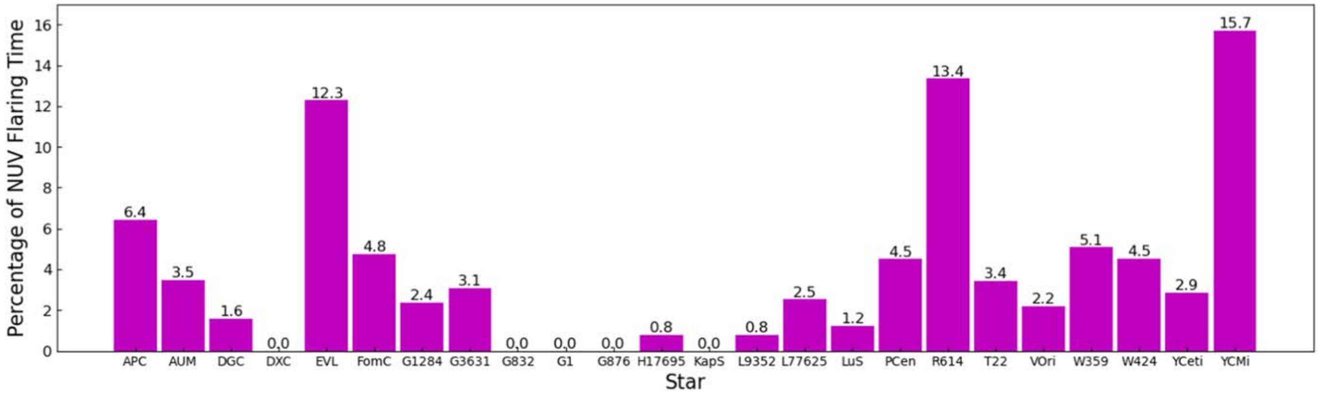

Figure 7. Swift NUV flaring fraction of observing time for each star in the sample. The names of stars are given in abbreviated form and are in the same order as in Table 1.

observed on M4−M6 dwarfs had optical counterparts in the energy bins $10^{27}-10^{29}$ erg, $10^{29}-10^{31}$ erg, and $10^{31}-10^{33}$ erg, respectively. Overall, 28% and 23.4% of NUV flares observed on M0−M3 and M4−M6 dwarfs had optical counterparts, respectively.

We also estimated the number of optical flares observed on our targets during the Swift/UVOT observation windows, which had NUV counterparts. We found that a total of 65 optical flares were observed by TESS/K2 simultaneously with Swift/UVOT. We confirmed this by visually inspecting the light curves. It is interesting to note that all except two of them had NUV counterparts. In addition to the 51 NUV flares discussed above, Swift/UVOT observed a very small fraction of the rise/decay phase of an additional 14 flares during the start/end of a given observing window. This is confirmed by an elevation in the NUV flux in the light curves of the stars and is demonstrated in the right panel of Figure 6. Such flares are not used for further analysis in this paper since we have very limited information about their properties. However, taking into account those 14 additional events, the total number of NUV flares we observed on our stars is 227, among which 65 (∼29%) had optical counterparts.

Surprisingly, the likelihood of an NUV flare occurring alongside an optical flare is very high. Conversely, the probability of an optical flare accompanying an NUV flare is notably lower, around 28%. Examples of NUV flares lacking optical counterparts, as depicted in the left and middle panels of Figure 6, indicate that the combination of the cadence of optical sampling and the relatively low flare amplitude may be the primary factors limiting the detection of optical flare counterparts. In the provided examples, there are observable signs of flux increase in the TESS light curves during NUV flares. However, these signs do not manifest as distinct flares in the light curves, as they are diluted within the noise of the light curves.

4. Results

4.1. Flaring Rates and Durations

In Figure 7 we present the NUV flaring fraction time for each star in our sample based on the duration of all flares observed (listed in Table 9) and the total observation time (listed in Table 2) of that star. EV Lac, Ross 614, and YZ CMi were in a flaring state for >10% of the observing time, a much greater percentage than the other stars. On the other hand, five stars (DX CNc, GJ 1, GJ 832, GJ 876, and Kapetyn's star) did not flare. This result applies to Swift observations only. On average, the NUV flaring time is 2.1% for M0−M3 dwarfs and 5% for M4−M6 dwarfs. However, this fraction also depends on the age of the stars since they tend to show different flaring behaviors in various ages.

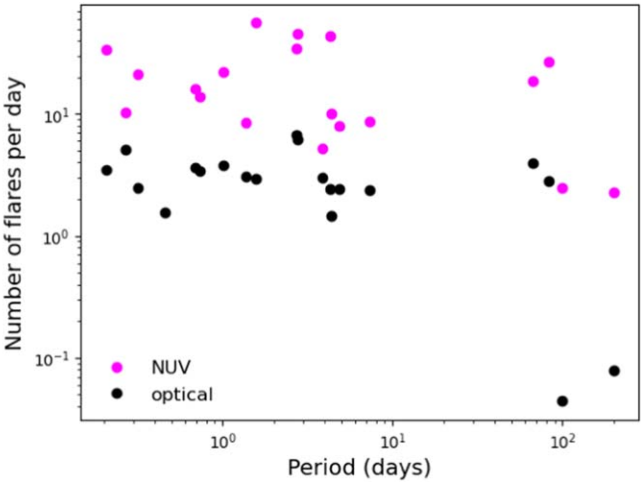

Figure 8. Flare rates as a function of rotation periods of stars. The magenta circles correspond to NUV flares, and the black circles correspond to optical flares.

Almost all NUV flares in this study were observed on known active M dwarfs. However, the occurrence of two NUV flares on the optically inactive M dwarf GJ 832 (approximately 8.4 Gyr old) in HST/STIS band indicates that even inactive M dwarfs can produce NUV flares. This is in agreement with the findings from X-ray and FUV wavelengths for GJ 832 and other optically inactive M dwarfs (Loyd et al. 2018). The detection of two short-duration flares in the HST light curve, with an exposure time of only ∼12 ks (shorter than most of the Swift/UVOT observations), suggests that observing optically inactive M dwarfs requires instruments with greater sensitivity than Swift/UVOT. Such stars exhibit very low count rates in Swift/UVOT light curves, which limits our sensitivity to the energies of very small flares.

Next, we investigate whether there is any correlation between the rotation period and the NUV/optical flare rates of stars. Our analysis includes only those stars that exhibited at least one flare in both NUV and optical passbands. The flare rate of each star is calculated as the ratio of the total number of flares observed in a given passband to the total observation time in that same passband. Figure 8 shows no discernible relationship between the rotation period and flare rates for both NUV and optical passbands. Interestingly, the NUV flare rates consistently appear to be higher than the optical flare rates in all cases. However, we must consider potential biases that could affect these results, specifically related to the differences in the cadence size used for identifying flares in NUV and optical observations. Shorter cadences are crucial for detecting very small flares that last for only a few tens of seconds. Additionally, the contrast between flaring and quiescent states is much larger in the NUV than in the optical; this also aids in detection of NUV flares.

In Figure 9, we explicitly compare the flare durations as measured in the NUV and optical. For this comparison, we used only the sample of flares that were observed by TESS in 20 s cadence mode and have detected NUV counterparts. The three longest-duration flares were observed on AP Col, YZ CMi, and GJ 3631. The duration of NUV flares is in the range of 0.37−23.0 minutes, and that of TESS flares is in the range of 0.62−47.3 minutes. The black dashed line in Figure 9 represents the case when the durations of both optical and NUV flares are equal and is not a fit. It is evident from the plot that many of the flares do not show similar durations between the bands; there are more flares with longer NUV flare durations than longer optical flare durations. We need a bigger sample of flares observed by using similar cadence size in both bands to verify that the NUV flares tend to have longer durations than the optical flares. We also note that Kawai et al. (2022) found a linear duration between e-folding times of soft X-ray (SXR) and Hα light curves in the decay phase of flares for a time range of 1–10^4 s. In Figure 10, we plot the NUV flare durations against the corresponding NUV flare energies, limiting only to those flares that were observed for their full duration and with 20 s TESS data in order to minimize the disparity in cadence size between Swift NUV data and TESS data. Next, we compare the trends in durations and integrated energies of all optical and NUV flares studied here with other stellar and solar flare studies in Figure 11. To convert NUV flare energies to bolometric energies, we utilized the ratio $E_{\rm NUV}/E_{\rm bol} = 0.217$. This ratio is based on the ratio of bolometric flare energy to TESS band energy (for a 10,000 K BB) discussed in Section 3.1.2 and the ratio of energies in TESS and Swift NUV (UVM2) band for the best RHD model predicting NUV flare energies from TESS flare energies as discussed in Section 4.3.3.

The solar and stellar flares used in Figure 11 were observed with Solar Dynamics Observatory (SDO)/Helioseismic and Magnetic Imager (HMI; Namekata et al. 2017), GALEX (Brasseur et al. 2019), the Dark Energy Camera (DECam; Webb et al. 2021), and Kepler (Shibayama et al. 2013; Maehara et al. 2015). The DECam flares were observed on stars at distances up to 500 pc as part of DECam's Deeper, Wider, Faster program (Andreoni & Cooke 2019). However, we do not have information regarding the types of stars in the DECam sample. The Kepler flares, on the other hand, were all observed on solar-type stars.

Figure 11 also shows the expected relationship between flare duration and energy for emitting regions with a uniform magnetic field strength (B) but varying length scale (L). This is represented by forward-slanted dotted lines. Likewise, the backward-slanted dashed lines represent the expected relationship in the case of uniform L but varying B (Namekata et al. 2017). These laws were formulated by equating the flare duration (τ) to the reconnection timescale ($\tau_{\rm rec}$) and establishing a relationship between flare energy (E) and the magnetic energy ($E_{\rm mag}$) released, while eliminating either the length scale or the magnetic field strength.

We can see that the majority of the M dwarf NUV flares have energies and durations comparable to the solar white-light flares. Some of them even have energies and durations smaller than those of solar flares, the smallest being 2.6×10^{28} erg and ∼0.3 minutes. Likewise, ∼50% of M dwarf optical flares have energies greater than those of the solar white-light flares. The grouping of the NUV and optical M dwarf flares around the solar flares indicates that both solar and M dwarf flares follow a common scaling law between the flare duration and energy. This suggests that a common mechanism of magnetic reconnection produces both solar and M dwarf flares. Interestingly, our M dwarf NUV and optical flares have durations comparable to the GALEX, Kepler short-cadence, and DEC flares yet far lesser energies.

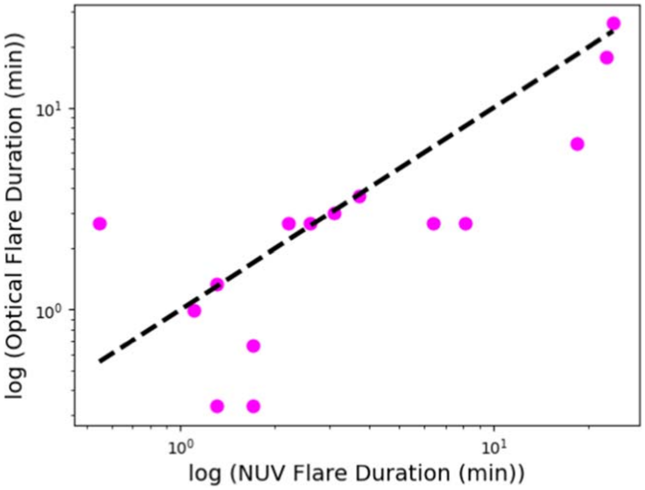

Figure 9. Comparison of NUV flare durations with those of the corresponding optical counterparts. For the most accurate comparison, we used only the sample of 15 flares that were observed by TESS in 20 s cadence mode. The black dashed line represents the case when NUV and optical flare durations are equal for each flare.

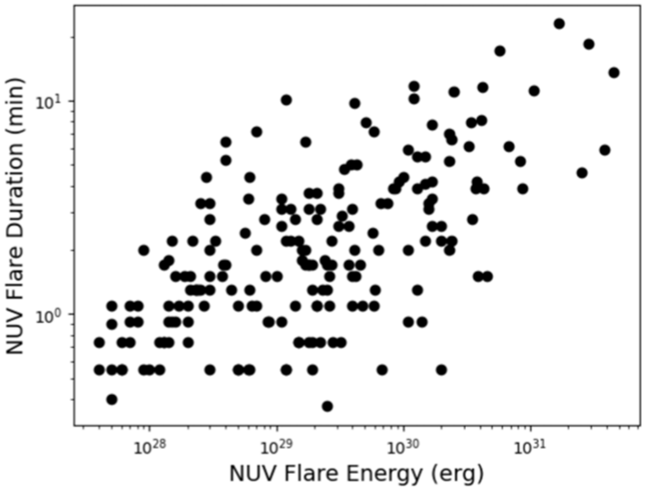

Figure 10. Duration of NUV flares vs. the corresponding NUV flare energies. Only the sample of NUV flares observed for full duration is used for this plot.

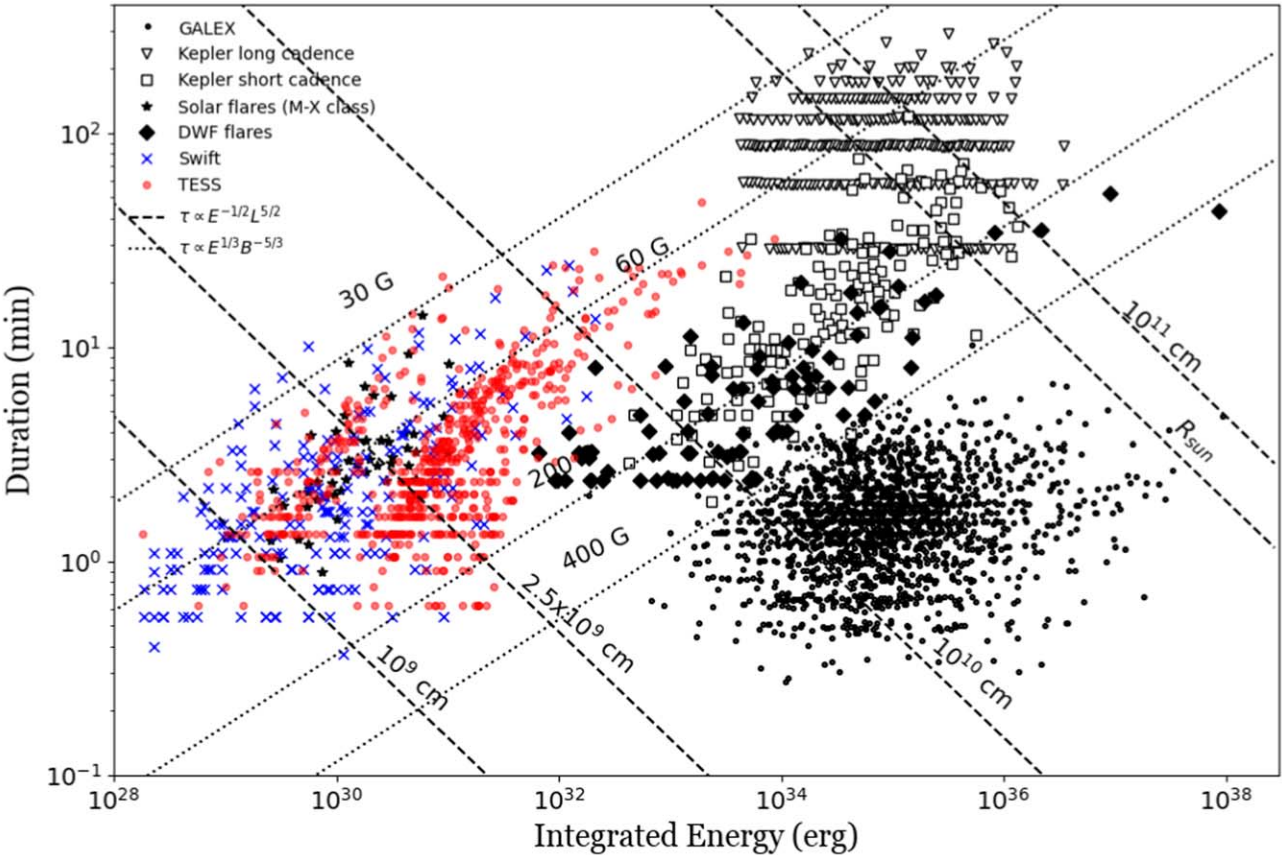

Figure 11. Comparison of bolometric energies and durations of NUV (blue crosses) and optical (red circles) M dwarf flares from this work with those of solar and stellar flares observed with SDO/HMI (black filled stars; Namekata et al. 2017), GALEX (black asterisks; Brasseur et al. 2019), DEC (filled diamonds; Webb et al. 2021), and Kepler (open triangles and open squares; Shibayama et al. 2013; Maehara et al. 2015). The cadence sizes are 45 s, 10 s, 20 s, and 1 or 30 minutes, respectively. The dashed and dotted lines correspond to scaling laws between flare durations and energies corresponding to either constant magnetic field (*B*) with varying emitting region length scale (*L*) or constant emitting region length scale with varying magnetic field.

4.2. Flare Amplitudes

Figure 12 shows the distributions of amplitudes relative to quiescence for both NUV and TESS/optical flares. We used the sample of TESS flares observed in 20 s cadence mode to ensure greater accuracy, because flare amplitudes can be underestimated when using longer-cadence data. Among the 213 NUV flares, 209 (98%) have amplitudes greater than 1.5×, and 198 (93%) have amplitudes greater than 2× the quiescent flux. Among the 655 TESS flares, 280 (43%) have amplitudes less than 1%, 445 (68%) have less than 2%, and 539 (82%) have less than 5% of the quiescent flux. Furthermore, we estimate that the mode of NUV flare amplitudes is 2.1, while the mode of optical flares is 1.004; both amplitudes are expressed relative to the corresponding quiescent levels. This discrepancy between NUV and optical flare amplitudes arises because M dwarfs have low levels of quiescent UV fluxes, so the contrast between quiescent and flaring periods is far greater than in the optical.

Next, we compare the amplitudes of flares that were observed simultaneously by both Swift and TESS (20 s cadence only) in Figure 13. It is evident that all optical flares, except one, have peak fluxes that are $\lesssim$2.5% higher than the quiescent flux. However, the NUV counterparts exhibit very large peak fluxes, reaching levels as high as ~70× the quiescent flux.

Since the mid- to late M dwarfs and L dwarfs are redder than early M dwarfs, the optical flares exhibit higher amplitudes in the case of such stars with peak fluxes sometimes exceeding 100 times the quiescent flux (see, e.g., Paudel et al. 2020, 2018a). In addition to this, results in Section 3.3 suggest that almost all optical flares have NUV counterparts. This might be why we observed the highest number of optical counterparts (totaling 18) on Wolf 359 (an M6 dwarf) compared to the other stars in our sample. Wolf 359 also has a high flare rate, and it was observed by Swift for a longer duration than other stars.

Our results regarding the flare durations and amplitudes suggest that one of the reasons for the lack of optical counterparts to NUV flares in G–K stars pointed out by Brasseur et al. (2023) might be the cadence size mismatch between GALEX data and Kepler data, rather than any physical process. The results in Section 3.3 strongly support this claim. Brasseur et al. (2019) reported that the majority (98%) of the GALEX flares studied in Brasseur et al. (2023) had durations less than 9 minutes, and there were very few flares with durations on the order of 10 minutes. They used 10 s cadence GALEX data and contemporaneous Kepler long-cadence (30 minute) data, except for two flares which had Kepler short-cadence (1 minute) data, to search for optical counterparts to 1559 GALEX flares.

The next possible reason might be very low amplitudes of optical flares in G–K stars. This is also evident from the M dwarf flares we observed simultaneously with Swift and TESS. Even though they have cadence sizes closer than any existing

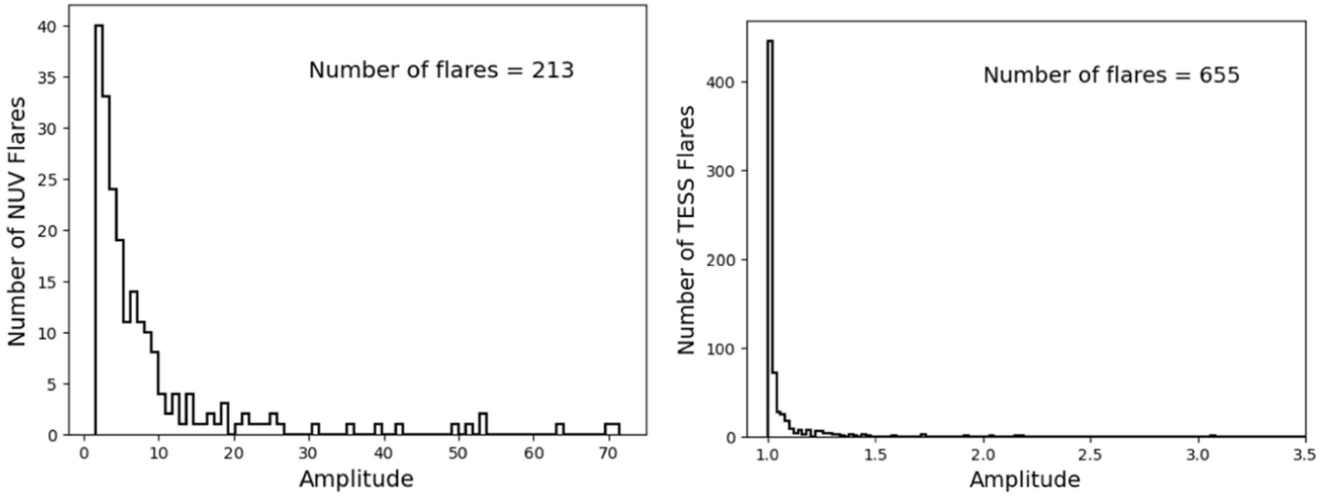

Figure 12. Histogram of flare amplitudes, i.e., the peak flare fluxes measured relative to the quiescent flux of the flaring star, measured in the NUV with Swift (left panel) and optical with 20 s TESS data (right panel).

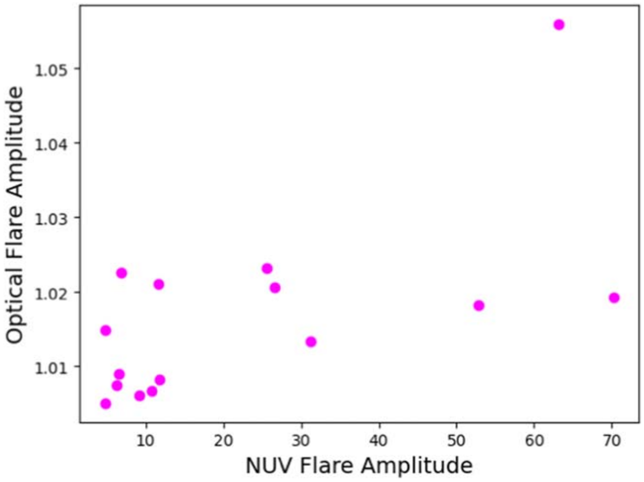

Figure 13. Comparison between amplitudes of NUV and optical flares observed simultaneously with Swift and TESS (20 s cadence only).

data, we found that the optical flares have significantly lower amplitudes compared to their NUV counterparts (see Figure 13). Since G–K dwarfs are optically brighter than M dwarfs, the amplitudes of the optical flares produced by G–K stars would be smaller than those of M dwarfs and hence might be diluted by the noise in the data. However, the results of Brasseur et al. (2023) require confirmation through a larger sample of G–K flares observed simultaneously in optical and NUV bands using similar cadence sizes, as well as more sensitive optical telescopes capable of capturing flare amplitudes in G–K stars to less than 0.1%.

Table 6
Flare Models and Energy Ratios between Bandpasses

Model	TESS/Swift Ratio	Kepler/Swift Ratio
F13	0.741	1.460
F13+2.5*5F11	0.760	1.486
F13+5.0*5F11	0.778	1.510
F13+7.5*5F11	0.795	1.534
F13+10.0*5F11	0.812	1.557
F13+12.5*5F11	0.828	1.579
5F11	1.886	3.029
9000 K BB	2.648	4.704
18,000 K BB	0.296	0.661
36,000 K BB	0.114	0.283

4.3. NUV/Optical Energy Fractionation

4.3.1. Expectations from Flare Models and Previous Observations

A single-temperature BB model is insufficient in explaining certain observed features in flare spectral energy distributions, such as the Balmer jump and emission/absorption lines. In order to address this limitation and provide a more realistic representation of stellar flare spectral energy distributions, Brasseur et al. (2023) employed a range of RHD models using the RADYN code (Carlsson & Stein 1992, 1995, 1997; Allred et al. 2015) to investigate the energy fractionation between TESS/Kepler and GALEX bandpass energies. Specifically, they utilized different combinations of two RHD models, namely F13 and 5F11 (where the last two digits denote the logarithm of the electron beam flux), to more accurately reproduce the optical and NUV spectra of M dwarf flares. The M dwarf flares exhibit continuum enhancements spanning from ultraviolet to optical wavelengths, along with an additional continuum component beyond the Hβ wavelength ($\geqslant$4900 Å; Kowalski et al. 2013). The two flare models use injected electron beams with differing properties, like maximum fluxes and low-energy cutoffs, to reproduce both features. The F13 flare model demonstrates increased blue continuum emission characterized by a color temperature exceeding 9000 K, while the 5F11 model displays a more pronounced Balmer jump ratio. The two models are combined using a relative filling factor, $X_{5\mathrm{F}11} = 0$–12.5. The combined model incorporates the increase in both Balmer jump ratio and Balmer line flux without disrupting the flare color temperature, thereby aligning with spectral observations of M dwarf flares within the blue–optical wavelength range. For more comprehensive information on these models, we refer the reader to Brasseur et al. (2023). We compare these models to our observed flux ratios between the TESS optical and Swift NUV bandpasses. Table 6 provides a summary of the model names, along with the corresponding expected energy ratios $E_{\mathrm{TESS}}/E_{\mathrm{Swift}}$ and $E_{\mathrm{Kepler}}/E_{\mathrm{Swift}}$. These energy ratios were calculated using the total luminosity within

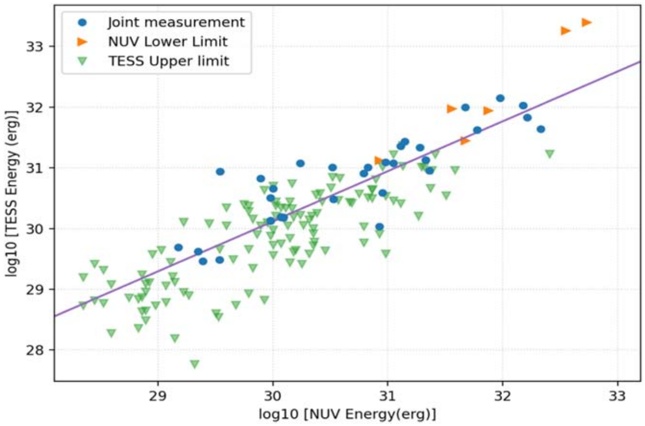

Figure 14. Observed NUV flare energies vs. observed TESS flare energies. The blue circles represent the flares that were observed simultaneously by both TESS and Swift/UVOT for their full duration. The orange rightward-pointing triangles right represent the flares that were not observed for the full duration by Swift/UVOT but have optical counterparts. The green downward-facing triangles represent the NUV flares with upper limits on the TESS flare energies. The blue line represents the linear fit with the form log $E_{\mathrm{TESS}} = 0.823 \pm 0.059$ log $E_{\mathrm{NUV}} + 5.630 \pm 1.8$.

each band (see Equation (2) of Tristan et al. 2023) and assuming identical flaring durations between bands. The TESS and Kepler fluxes were calculated by integrating the model spectra with the filter response functions, following the method outlined in Sirianni et al. (2005).

4.3.2. Empirical Relation between E_{NUV} and E_{TESS}

We calculated an empirical relationship between our observed NUV and TESS flare energies (Figure 14). We included in the model the upper limits on the TESS energies for the NUV flares without optical counterparts in the TESS data, as well as lower limits on the Swift flare energies for incomplete flares. We note that the TESS flare energies (E_{TESS}) are estimated by converting the bolometric flare energies, obtained for a 10,000 K BB from Equation (2), to TESS band energies using the energy ratio $E_{\mathrm{TESS}}/E_{\mathrm{bol}} = 0.18$, as given in Section 3.1.2. We performed a linear regression analysis on the logarithmic data and obtained a relationship of the form log $E_{\mathrm{TESS}} = 0.823 \pm 0.059\ E_{\mathrm{NUV}} + 5.630 \pm 1.8$. We refer to this fit as the PL fit in the following sections. We considered other functional forms, such as a quadratic relation, but found that the linear relationship in log–log space (e.g., a power law) better fits the data. Using the PL fit results, we predicted the NUV energies based on the observed TESS energies. We compare those predicted NUV energies with the observed NUV energies in Figure 15(a). The residual plot in the bottom of Figure 15(a) indicates that the NUV energies estimated from TESS energies, utilizing the PL fit results, align moderately well with the observed values. It is important to note that some scatter may result from a potential mismatch in the cadence size of NUV and TESS data.

4.3.3. Choice of Best Model for Predicting E_{NUV} Using E_{TESS}

Due to the distinct spectral characteristics of M dwarf flares, our primary interest lies in determining the most suitable fit among the five available hybrid models. This is in contrast to opting for a single-temperature BB model or models exhibiting significant enhancements solely in the continuum (F13 model) or solely in the Balmer jump ratio (5F11 model). Consequently, our focus remains exclusively on hybrid models.

To assess the optimal hybrid model among the five presented in Table 6, we calculate NUV energies from the observed TESS energies using the energy ratios associated with all five hybrid models listed in the same table. For this, we used the sample of flares that were observed simultaneously by both TESS and Swift/UVOT for the full duration. Subsequently, we carried out four statistical tests: the Kolmogorov–Smirnov (K-S) test, the Anderson–Darling test, the Bayesian information criterion (BIC), and the Akaike information criterion (AIC) to ascertain the model that fits the data best. A summary of the results from these statistical tests is provided in Table 7. We also include the statistical tests for the results of the PL fit for comparison with those of hybrid models. We can see that the K-S test and AD tests are inconclusive for all models. However, the BIC and AIC values are somewhat different for each model, and the lowest value determines the best model. Here the model F13+12.5*5F11 has the lowest value of both BIC and AIC, so we consider it to be the best among the five hybrid models.

4.3.4. Comparison between PL Fit, 9000 K BB, and F13+12.5*5F11 Hybrid Model

Next, we compared the observed NUV flare energies with those predicted from TESS/K2 flares using the PL fit, 9000 K BB,[20] and F13+12.5*5F11 hybrid model for the sample of flares that were simultaneously observed by TESS/K2 and Swift/UVOT throughout their complete durations. The comparisons are shown in panels (a), (b), and (c) of Figure 15. We included a comparison with the 9000 K BB model, aiming to provide readers with insight into its distinctions from the hybrid model and the PL fit. This particular model is widely used in the literature for predicting NUV flare energies based on optical flare energies. Some scattering of the data points in the top panels of the two plots might be due to a mismatch in the cadence size between the TESS and NUV data, leading to differences in the accuracy of the estimated energy values in the two bands.

The flare energies predicted by the two models (9000 K BB and F13+12.5*5F11) differ by a factor of 3.2 (see Table 6). Hence, we do not see distinct differences in the top panels of the two plots. However, we see some difference in the corresponding residual plots. The expected NUV flare energy versus observed NUV energy plot and residual plot in Figure 15(b) suggests that the 9000 K BB model is able to predict the NUV flare energies with values of less than 10^{30} ergs with more accuracy than those with energies greater than 10^{30} ergs. We estimate that it underestimates the NUV flare energies with values greater than 10^{30} ergs by a factor of ∼2.5, which is based on the median of differences in the observed and predicted NUV energies with values greater than 10^{30} ergs. Likewise, the expected NUV flare energy versus observed NUV energy plot and the residual plot in Figure 15(c) suggests that the F13+12.5*5F11 model is able to predict the energy of flares with values greater than 10^{30} ergs with more accuracy than those with energies less than 10^{30} ergs. We estimate that it overestimates the NUV flare energies with values less than 10^{30} ergs by a factor of ∼2.9, which is based on the median of

---

[20] It is chosen instead of 10,000 K BB here because we have used the same RHD models as those in Brasseur et al. (2023).

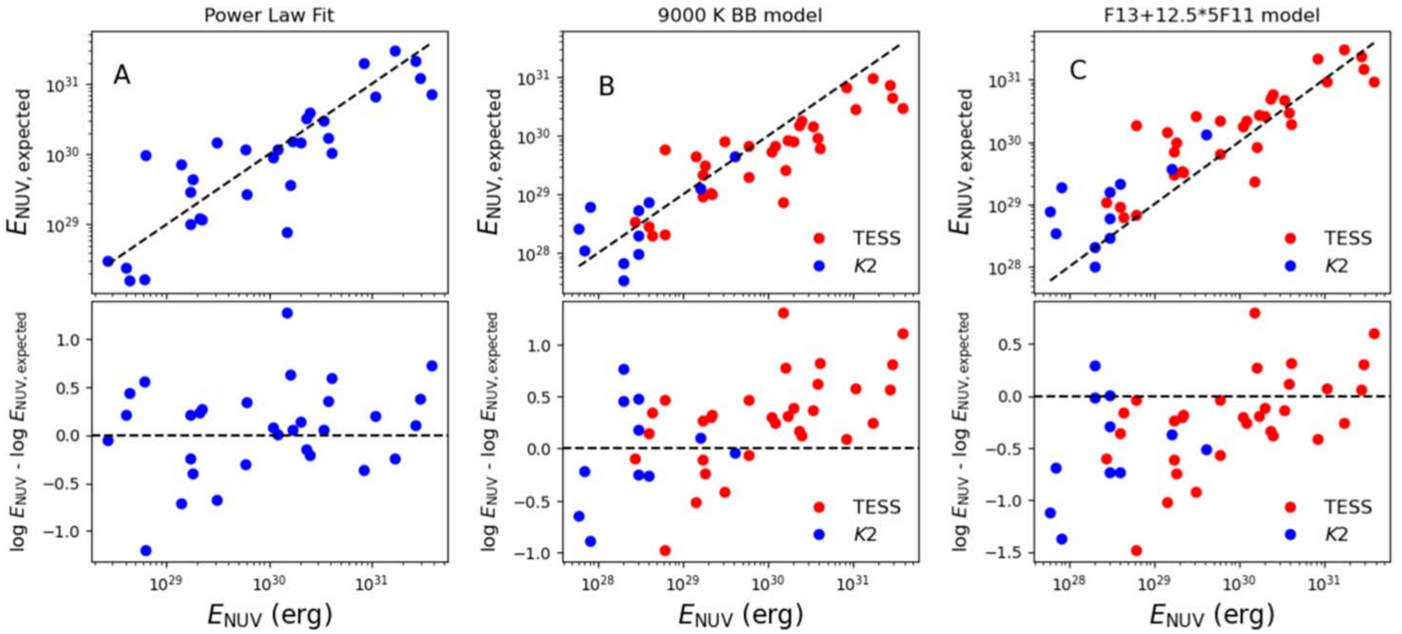

Figure 15. (a) Top: comparison of observed NUV flare energies with those predicted from fitting of the observed TESS flare energies, i.e., PL fit. Bottom: differences in logarithm of observed and expected NUV flare energies vs. the observed NUV flare energies. (b) Same as panel (a), but for the 9000 K BB model. (c) Same as panel (a), but for the F13+12.5*5F11 hybrid model. The slanted dashed line in the top panels and the horizontal dashed line in the bottom panels represent the case when the expected NUV energy is equal to the observed NUV energy.

Table 7
Results of Statistical Tests. I

Model	K-S Test	AD Test	BIC	AIC
F13+2.5*5F11	0.25,0.27	0.70,0.17	73.2	71.7
F13+5.0*5F11	0.25,0.27	0.70,0.17	71.7	70.3
F13+7.5*5F11	0.25,0.27	0.60,0.19	70.3	68.9
F13+10.0*5F11	0.25,0.27	0.59, 0.19	69.0	67.5
F13+12.5*5F11	0.25,0.27	0.51, 0.21	67.7	66.3
PL fit	0.09,0.999	−0.93, 0.25	63.2	61.7

Note. Among the two numbers listed in the K-S test and AD test, the first number is the statistic and the second number is the *p*-value.

differences in the observed and predicted NUV energies with values less than 10^{30} ergs.

4.3.5. E_{TESS}/E_{NUV} *versus* E_{NUV}

Similar to the study conducted by Brasseur et al. (2023), which utilized overlapping GALEX and Kepler data, we investigate the relationship between NUV and optical flare energies using simultaneous TESS and Swift/UVOT data. One advantage we possess over their investigation is a larger sample of flares that were identified in both TESS and Swift/UVOT light curves. We have a total of 31 NUV flares that were observed for the entire duration by both telescopes and were identified in both light curves. Additionally, six more NUV flares were identified in both light curves, but they were not observed for the complete duration by Swift/UVOT. The remaining NUV flares were not identified in TESS light curves, and we derived upper limits on their TESS flare energies.

In the left panel of Figure 16, we present a plot of the ratio of TESS to Swift NUV energy ($E_{\rm TESS}/E_{\rm NUV}$) as a function of Swift energy ($E_{\rm NUV}$), utilizing only the energies of NUV flares that were observed for the entire duration by Swift and had optical counterparts identified in TESS light curves. For comparison purposes, we also overlay the K2 flare energies and their corresponding ratios with NUV energies. To assess any potential correlation between $E_{\rm TESS}/E_{\rm NUV}$ and $E_{\rm NUV}$, we fit a line log $E_{\rm TESS}/E_{\rm NUV} = -0.289 \pm 0.080$ log $E_{\rm NUV} + 8.797 \pm 2.383$ by excluding K2 data. The fit is represented by the black solid line. The fit to the data was obtained using `pymc3`, revealing a slight decreasing trend in the energy fractionation as the NUV flare energy increases. The corresponding residuals are shown in the bottom plot of the left panel. A more pronounced decreasing trend was observed in the higher GALEX flare energies studied by Brasseur et al. (2023). The main distinction between the two studies is that the flare energies in Brasseur et al. (2023) were in the range log *E* (erg) ∼ 32–36, whereas in this study the flare energies have values in the range log *E* (erg) ∼ 28–32. We want to remind the readers about the different stellar populations being probed in this paper versus Brasseur et al. (2023). While the sample of stars is all M dwarfs in this study, it is mostly G–K dwarfs in Brasseur et al. (2023) except one. They included additional literature values of M dwarf flares that spanned a wider range of energies than solar flares, and they suggested that M dwarf flares might have energy fractionations closer to what the Sun exhibits at lower energies.

Next, we examined the energy fractionation using the entire sample of NUV flares. The right panel of Figure 16 illustrates the relationship between the two energies for this case. The fitted line has the form log $E_{\rm TESS}/E_{\rm NUV} = -0.177 \pm 0.060$ log $E_{\rm NUV} + 5.40 \pm 1.80$, and hence we find that the correlation is even weaker compared to the aforementioned case. The corresponding residuals are shown in the bottom right panel. This fit includes the upper and lower limits in the observed TESS and Swift data sets.

Observations in Kowalski et al. (2013) demonstrated that there was a systematic dependence of the amount of excess Balmer continuum emission above a linear fit to the BB component; the ratio of the two continuum fluxes decreases as the flare luminosity increases. This suggests that for low-to-

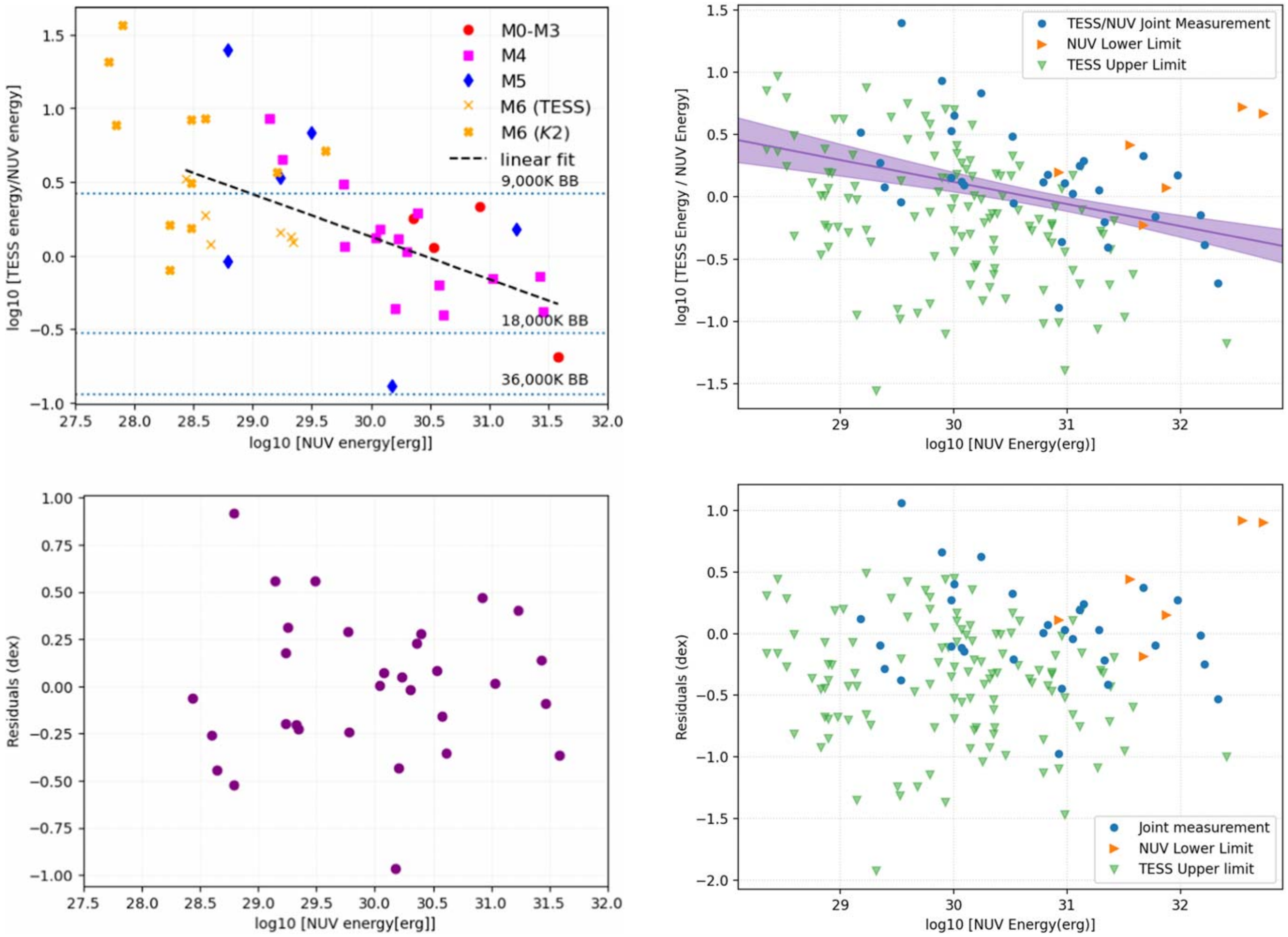

Figure 16. Top left: energy fractionation between TESS and Swift NUV flare energies for a sample of 31 NUV flares that were observed for the entire duration by Swift and had optical counterparts identified in TESS light curves. The data points are classified by spectral type of the stars on which the flares were observed. The black solid line represents the PL fit to the data. This line shows that there is a slight decreasing trend in the energy fractionation as the NUV flare energy increases. Additionally, the K2 flare energies and their corresponding ratios with NUV energies are overplotted for comparison. The dotted horizontal lines correspond to the anticipated energy fractionation for BBs at temperatures of 9000, 18,000, and 36,000 K. Bottom left: corresponding residuals of the top left panel. Top right: energy fractionation between TESS and Swift NUV flare energies for the entire sample of NUV flares in this study. The purple circles represent the energies of NUV flares that were observed for the entire duration by Swift and had optical counterparts identified in TESS light curves. The triangles represent the energies of NUV flares that either were not observed for the complete duration by Swift or lacked optical counterparts in TESS light curves. The purple solid line represents the PL fit to the data, and the shaded region represents the 1σ uncertainty on the fit. Bottom right: corresponding residuals of the top right panel.

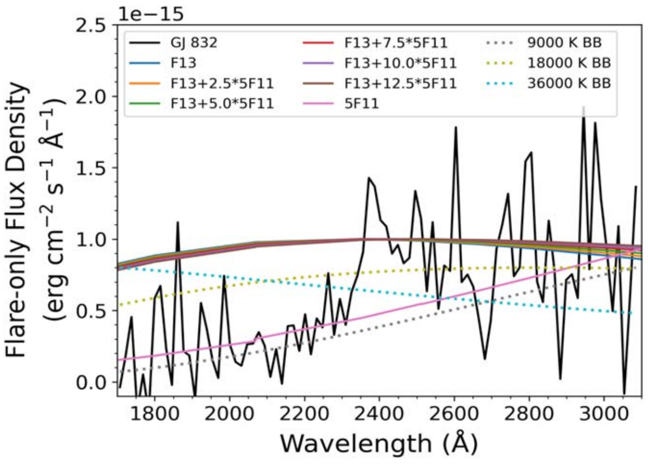

Figure 17. Comparison of the GJ 832 NUV flare-only spectrum (black line; binned to 15 Å for improved signal-to-noise ratio) with the model spectra discussed in Section 4.3.1. The model spectra have been scaled for visual comparison of the spectral shapes.

moderate-luminosity flares the larger component of NUV emission, on top of any BB emission, would show up as a larger energy fractionation between the NUV and optical bandpasses. Kowalski et al. (2016) also demonstrated that moderate-to-high-luminosity flares have smaller Balmer jump ratios and hotter color temperatures, which would also suggest a systematic behavior in energy fractionation between the NUV and optical bandpasses.

4.3.6. Comparison of Models with HST/STIS NUV Spectra

We analyzed the NUV spectral energy distribution of the first GJ 832 flare by subtracting the mean quiescent spectrum from the flare spectrum (Section 3.2.2) to generate a "flare-only" spectrum, shown in Figure 17. The flare-only spectrum is dominated by emission lines with no clear evidence of strong continuum emission. The majority of the flare emission occurs between 2200 and 3000 Å from a forest of Fe II emission lines and the Mg II *h* and *k* emission lines.

Table 8
Summary of Power-law Fits to FFDs

Sp. Type	NUV				Optical			
	β_{NUV}	N_{NUV}	log E_{min} (erg)	log E_{max} (erg)	β_{optical}	N_{optical}	log E_{min} (erg)	log E_{max} (erg)
M0−M3	-0.62 ± 0.15	18	30.2	32.0	-0.71 ± 0.05	225	31.0	33.6
M4−M6 (TESS 20 s)	-0.55 ± 0.08	44	28.5	31.5	-0.76 ± 0.04	362	29.5	32.5
M4−M6 (TESS 2 minutes + 20 s)	-0.59 ± 0.06	105	28.5	31.8	-0.80 ± 0.04	534	30.0	32.5
M4	-0.63 ± 0.07	76	29.0	31.5	-0.70 ± 0.03	666	30.0	33.4
M5	-0.61 ± 0.11	32	28.6	30.4	-0.67 ± 0.05	181	30.0	32.4
M6	-0.82 ± 0.13	39	28.0	29.6	-0.71 ± 0.06	137	28.5	31.2

Note. In this table, β_{NUV} and β_{optical} are the fitted slopes of FFDs, N_{NUV} and N_{optical} are the number of flares used for fitting, and E_{min} and E_{max} are the minimum and maximum energies used for fitting. The errors in the slopes are obtained by dividing the values of β by $\sqrt{N}$, where N is the number of flares used for fitting.

We also compared our flare-only spectra to the hybrid models discussed in Section 4.3.1 and find significant disagreement. This can be seen in Figure 17. The nonhybrid 5F11 model and the cooler 9000 K BB model best match the data but appear to be missing the Fe II and Mg II emission between 2300 and 2800 Å. This indicates that emission lines are an important component of some flare emissions, and these are not fully taken into account by the available RADYN models.

4.4. *Flare Frequency Distributions*

4.4.1. *FFD Generation and Fitting*

A power-law relationship has been observed in the cumulative distribution of flares for a flaring star. This relationship can be expressed as a linear equation: $\log \tilde{\nu} = C + \beta \log E$, where $\tilde{\nu}$ represents the cumulative frequency of flares occurring per unit time with energies higher than E. The values of the coefficient C and the spectral index β may vary for each individual star depending on its age and spectral type (Gershberg 2005; Lacy et al. 1976).

We used the maximum likelihood method described in Hogg et al. (2010) and implemented in the routine `emcee` (Foreman-Mackey et al. 2013) to fit a straight line to our data (in log scale) and hence obtain the optimal values of parameters β. To avoid bias, we neglected some low energies that show deviation from a power-law distribution for fitting in the case of both observed and predicted energies. The deviation is most likely due to instrumental sensitivity in detecting very weak flares. We also neglected the highest observed energies to reduce any bias in fitting. In some cases, particularly when the number of flares is small, we observe that the largest flare energy deviates from the straight line, leading to a change in the true value of the slope of the line, especially toward lower flare rates. We list the values of fitted parameters of flare frequency distributions (FFDs) in Table 8 for NUV flares and optical flares. Rekhi et al. (2023) also studied NUV M dwarf flares using archival GALEX data. However, they estimated that the slopes of the NUV FFDs were slightly less steep than the values we estimated in this study. One of the factors that might lead to different slope values could be the different energy ranges considered in the two studies. The range of NUV flare energies is approximately 10^{29}–10^{35} erg in Rekhi et al. (2023).

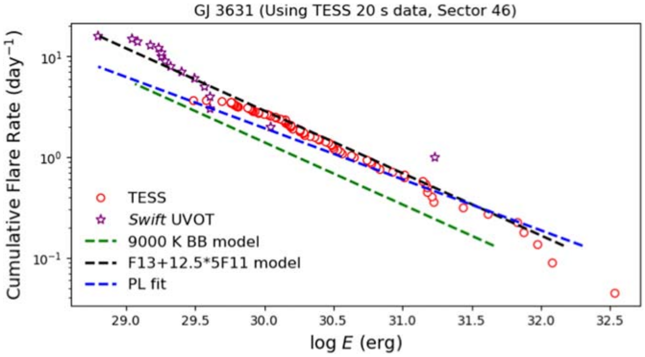

Figure 18. Frequency distribution of flares on GJ 3631 observed with TESS (red circles) and Swift/UVOT (purple stars) using the corresponding bandpass energies. The green, black, and blue dashed lines represent the linear fit to the frequency distribution of flares predicted using the 9000 K BB and F13 +2.5*5F11 models and the PL fit. All the fits are obtained by using the same range of TESS energies used for fitting. The blue and black dashed lines are extrapolated to the observed minimum NUV energy.

We aim to compare the FFDs of M dwarf flares observed by TESS and Swift/UVOT and those predicted from the TESS flare energies using the PL fit and the best hybrid model. This comparison will enable us to test the outcomes of the PL fit and the best hybrid model presented in Sections 4.3.2 and 4.3.3, respectively. To start, we focus on GJ 3631 as one of our targets, which has a high flare rate in both TESS and NUV passbands. During TESS Sector 46, we recorded 16 NUV flares with Swift/UVOT and 81 optical flares with TESS. Swift/UVOT and TESS observed this star for 86.1 ks and 22.2 days, respectively. The TESS data were collected in 20 s cadence mode. The FFD of GJ 3631 is depicted in Figure 18.

In the same figure, we compare the observed NUV FFD with those projected from optical flare rates using the 9000 K BB and F13+12.5*5F11 models and the PL fit. For our projections with the models and the PL fit, we first predicted the NUV FFDs from TESS energies using the energy ratios outlined in Table 6 and the results of the PL fit from Section 4.3.2. We then used a power law to fit those predicted NUV FFDs. Subsequently, we extrapolated these fitting outcomes to the minimum observed NUV energies. Thus, the dashed lines in Figure 18 represent the fits to the predicted NUV FFDs, not the direct prediction of the models and the PL fit. From the figure, we see that the F13+12.5*5F11 model predicts the NUV FFD with greater proximity to the observed NUV FFD compared to

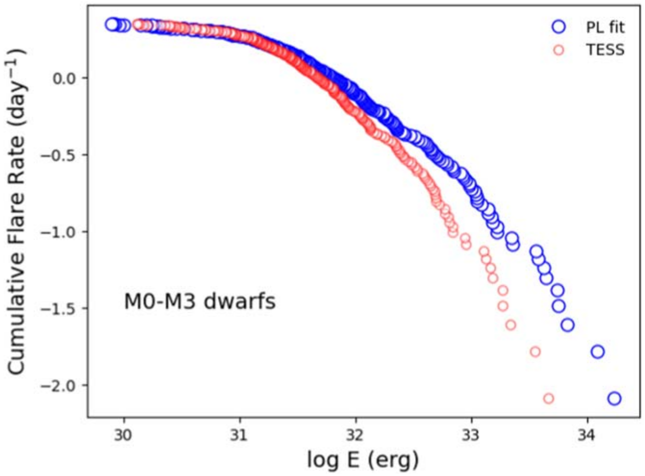

Figure 19. Comparison between observed TESS FFD of M0−M3 dwarfs and the FFD estimated by using the PL fit.

the prediction by the 9000 K BB model. We find that the fit of the NUV FFD predicted by the PL fit deviates from the observed distribution at lower energies for the cases when the sample of flares with energies $>10^{31}$ erg is small, and we show that it can predict the NUV FFD more accurately when the sample of flares with energies $>10^{31}$ erg is large as discussed in the following paragraph.

The minimum energy ($E'_{\rm min}$) used for fitting the predicted NUV FFDs is determined by the minimum energy $E_{\rm T,min}$ applied in fitting the observed TESS FFDs. If the predicted NUV FFD does not exhibit significant flattening at lower energies, similar to the observed TESS FFD, we use all predicted energies except the largest for fitting. However, if there is flattening, $E'_{\rm min}$ for the NUV FFD predicted by the BB and hybrid models is the energy corresponding to $E_{\rm T,min}$ using the energy ratio in Table 6. For the PL fit, $E'_{\rm min}$ is not solely the energy predicted from $E_{\rm T,min}$. The predicted value needs adjustment in cases where there are many flares with energies greater than 10^{31} ergs. This is because the PL fit predicts NUV energies with values lower than TESS energies for $\lesssim 10^{31}$ ergs and higher than TESS energies for $>10^{31}$ ergs. This is demonstrated in Figure 19. If the value of $E_{\rm T,min}$ is less than 10^{31} ergs, the new value of the minimum energy $E'_{\rm min}$ will be lesser than $E_{\rm T,min}$. Consequently, the slope of the FFD becomes less steep, given that the slope of the FFD depends on the range of energies chosen for fitting. The fitted NUV FFD based on this minimum may not accurately predict the observed high flare rates of lower NUV energies. While we are uncertain about adjusting the minimum value of the predicted NUV energy for FFD fitting correctly, we use a new value $E''_{\rm min}$, which is the average of $E'_{\rm min}$ and the NUV energy predicted by the PL fit corresponding to the largest TESS energy. This way the fitted FFD predicted by the PL fit is able to match the high flare rates of observed NUV flares with lower energies to some extent. This is the case when the sample of flares with energies $>10^{31}$ erg is large, and it is demonstrated in the FFDs shown in Figure 20.

4.4.2. FFD as a Function of Spectral Type

In this section, we analyze the FFDs of the M dwarfs in our sample as a function of spectral type in both NUV and optical passbands. We used a sample of M dwarfs with multiple flares

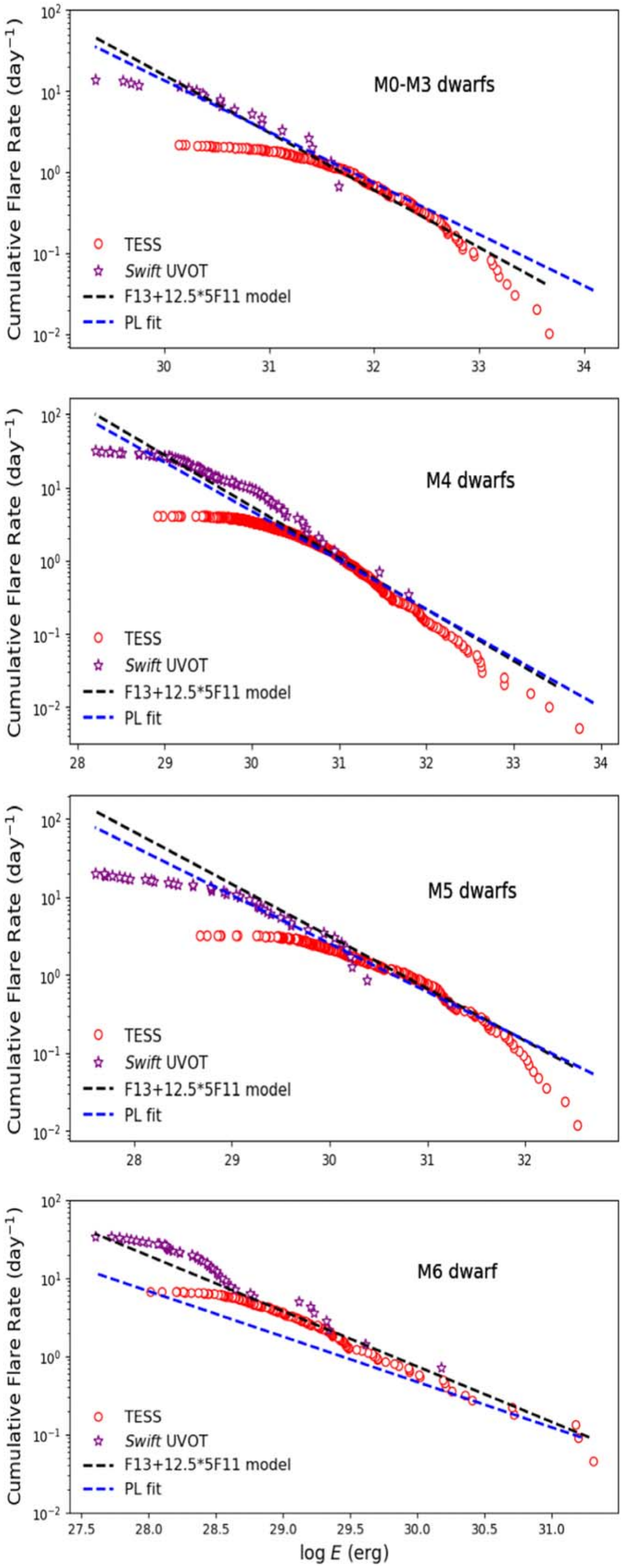

Figure 20. Cumulative frequency distribution of flares on M0−M3, M4, M5, and M6 dwarfs observed with TESS data (red circles) and Swift/UVOT data (purple stars), utilizing the respective bandpass energies. Additionally, the blue and black dashed lines correspond to the fit to the NUV FFD predicted by the PL fit and the F13+12.5*5F11 model from TESS FFD, respectively.

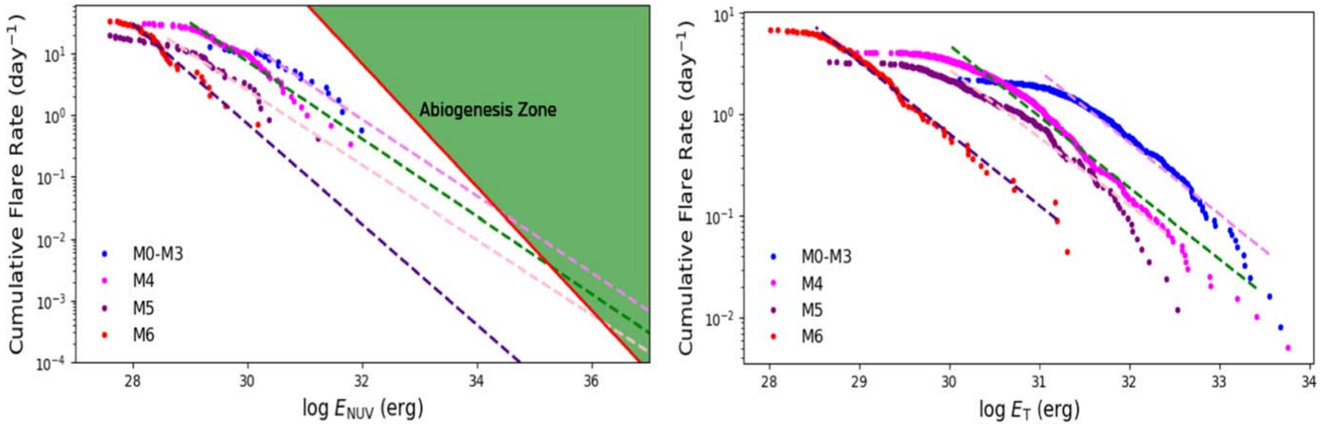

Figure 21. Left panel: frequency distribution of NUV flares as a function of spectral type. The circles represent the observed data, and the dashed lines are the linear fit to the FFDs. The FFDs of M0–M3, M4, and M5 have comparable slopes. The green area in the upper right corner corresponds to the abiogenesis zone estimated using the Rimmer et al. (2018) relation. This figure suggests that M0–M3, M4, and M5 dwarfs have NUV flare rates necessary for abiogenesis. However, the sample size of flares in each spectral type is small. Right panel: frequency distribution of TESS flares as a function of spectral type. The circles represent the observed data, and the dashed lines are the linear fit to the FFDs. The FFDs of TESS flares have steeper slopes compared to those of NUV flares. However, it is important to note that the range of energies used for fitting is different. We observe that both TESS and NUV flares follow a similar distribution trend as a function of spectral type.

in each spectral type. The sample consists of five M0–M3 dwarfs (AU Mic, EV Lac, GJ 1284, LP 776-25, V1005 Ori), seven M4 dwarfs (AP Col, DG CVn, Fomalhaut C, HIP 17695, Ross 614, YZ Ceti, YZ CMi), four M5 dwarfs (Proxima Centauri, GJ 3631, TWA 22, Wolf 424), and one M6 dwarf (Wolf 359) that exhibited multiple flares. We estimated the average FFD for each spectral bin. Due to the small number of flares in the early M dwarfs and the limited number of stars, we grouped M0–M3 dwarfs into a single bin. We note that we did not account for differing flare energy sensitivity and observation duration across various spectral types when grouping them into a single bin. The FFDs were fitted using the method described above. Additionally, we investigated the fits by combining M4–M6 dwarfs into a single bin to compare the FFDs between fully convective and partially convective M dwarfs, although the exact boundary between these two classes is hard to identify with spectral type alone. The results of FFD fittings for each spectral type and each energy band are summarized in Table 8. We also list the number of flares and the minimum and maximum energies used for fitting.

In Figure 20, we present the FFDs for each spectral type: M0–M3, M4, M5, and M6. Within each panel, a comparison is drawn between the observed NUV FFD and the observed TESS FFD, alongside the fit to NUV FFDs predicted from the TESS flare energies using the F13+12.5*5F11 model and the PL fit. The description of data points and lines is akin to that in Figure 18. As we are no longer interested in comparing the FFD estimated using the energy ratio of 9000 K BB, the corresponding fit to FFD for the 9000 K BB model is not depicted. Like the case in Figure 18, we find that the fit to the NUV FFD predicted by the PL fit deviates from the observed NUV FFD at lower flare energies in the case of an M6 dwarf, the reason for which is explained in Section 4.4.1.

Notably, this study represents the first time we can compare the FFDs of NUV and optical data using contemporaneous data. To visualize the results, we plotted the observed and the corresponding fitted FFDs of each spectral type for both NUV and TESS passbands in Figure 21, respectively. It is evident that the FFDs follow similar trends in both passbands. Specifically, the FFDs exhibit less steep slopes for NUV flares compared to TESS flares, and the slopes are consistent for all spectral types within the given errors. We also remind the readers that the values of slopes depend on the ranges of energies and the number of flares used for fitting. NUV flares are fitted for lower energy ranges, while TESS flares are fitted for higher energy ranges. Additionally, the number of flares used for fitting TESS flares is higher than that of NUV flares.

4.4.3. Abiogenesis

Rimmer et al. (2018) performed a study to investigate the influence of NUV light on the initiation of photochemical reactions that contribute to the formation of fundamental components necessary for the origin of life, known as abiogenesis. Their results are useful for exploring the possibility of emergent life on exoplanets located within the liquid-water habitable zones of various stars. They found that the application of NUV light within the wavelength range of 200–280 nm to a mixture of HCN and SO_3^{2-} resulted in the production of RNA pyrimidine nucleotide precursors. Conversely, the absence of NUV light in the same mixture led to the formation of inert adducts that lacked any prebiotic potential. Rimmer et al. (2018) defined the minimum NUV flux required for abiogenesis as the level of flux that initiates a 50% yield of the photochemical product. This minimum flux corresponds to a specific flux of 6.8×10^9 photons cm^{-2} s^{-1} Å^{-1} across the 200–280 nm wavelength band, which, upon integrating across those wavelengths, is equivalent to $F_{\rm min} \sim 45$ erg cm^{-2} s^{-1}. According to Rimmer et al. (2018), the minimum cumulative rate (ν) of flares at a given U-band energy (E_U) that satisfies the necessary yield is

$$\nu = \frac{8 \times 10^{27}\ {\rm erg\ s^{-1}}}{E_U}. \tag{5}$$

However, this equation is based on the assumption of the Great Flare of AD Leo in 1985 and its spectrum to calculate the number of photons cm^{-2} Å^{-1} and, hence, the NUV energy in the range of 200–280 nm. We no longer need to rely on this assumption, as we now have a good sample of NUV flares and our own estimation of NUV flare energies. Therefore, we use the NUV flare energies ($E_{\rm NUV}$) to constrain the abiogenesis

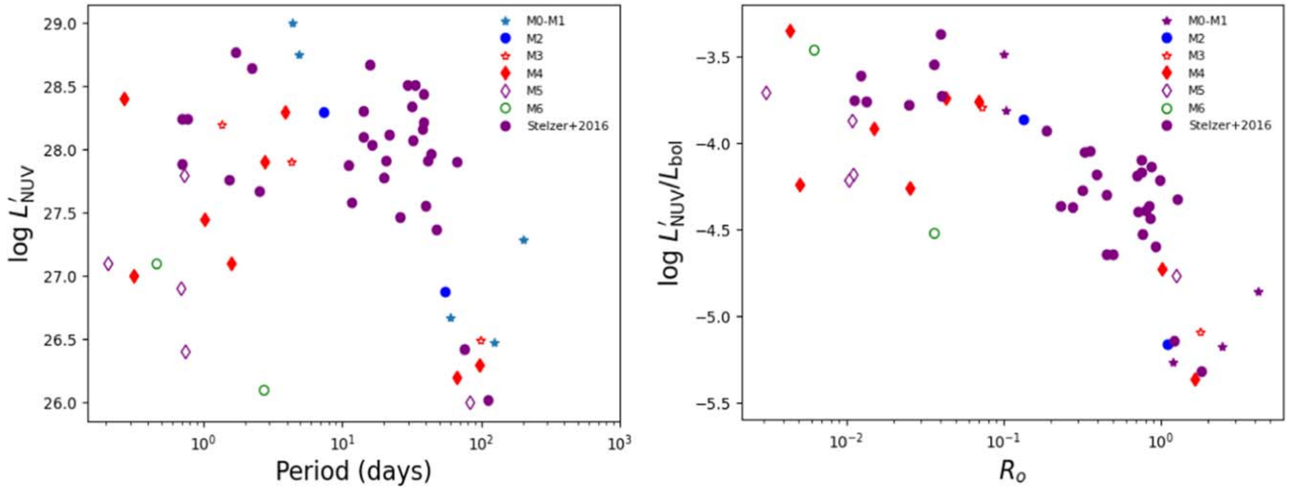

Figure 22. Left panel: excess NUV luminosity plotted against rotation period for M dwarfs. The purple circles represent the results from Stelzer et al. (2016). Left panel: excess NUV-to-bolometric luminosity ratio ($L'_{\rm NUV}/L_{\rm bol}$) plotted against the Rossby number (Ro = $P_{\rm rot}/\tau_{\rm conv}$). The purple circles represent the results from Stelzer et al. (2016).

zone and express the above equation as

$$\nu = \frac{6.9\times 10^{32}\ {\rm erg\ day}^{-1}}{E_{\rm NUV}}. \tag{6}$$

In the left panel of Figure 21, the green zone corresponds to the abiogenesis zone defined by Equation (6). In this figure, the fits to NUV FFDs of each spectral type are extrapolated to higher energies to see where they intersect the boundary line defining the abiogenesis zone. We observe that the fits to FFDs of M0−M3, M4, and M5 dwarfs intersect the line at NUV energies log $E\sim 34-36$ erg. Since M dwarfs are capable of emitting large flares with such energies (Lacy et al. 1976; Davenport 2016; Osten et al. 2016), the left panel of Figure 21 suggests that M0−M5 dwarfs can produce flares that could initiate abiogenesis while M6 might not be able to produce such flares. Since we have only one flaring M6 dwarf in our sample, we need a larger sample of stars with spectral type M6 to confirm this.

4.5. The NUV Activity–Rotation Relation

For the most rapid rotators, two crucial indicators of magnetic activity exhibit saturation. The first indicator, X-ray emission, is observed to saturate at values of $L_{\rm X}/L_{\rm bol}\approx 10^{-3}$ (Vilhu 1984; Micela et al. 1985; Pizzolato et al. 2003; Wright et al. 2011). Similarly, the second indicator, Hα emission, also saturates at values of $L_{\rm H\alpha}/L_{\rm bol}\approx 10^{-3.8}$ (Douglas et al. 2014; Newton et al. 2017). Here $L_{\rm X}$, $L_{\rm H\alpha}$, and $L_{\rm bol}$ represent the X-ray, Hα, and bolometric luminosity, respectively. Notably, this saturation phenomenon is observed irrespective of the stellar spectral type. Saturation is observed to set in at rotation periods of 1–10 days for solar-type stars and early M dwarfs, corresponding to Rossby numbers (Ro = $P_{\rm rot}/\tau$, where τ is the convective turnover time; Noyes et al. 1984) of order Ro $\sim$ 0.13 (Wright et al. 2011).

Stelzer et al. (2016) investigated the connection between rotation and chromospheric activity in a sample of 32 M dwarfs using GALEX NUV and K2 data. Among these stars, 13 exhibited slower rotation rates and had periods that were considered less reliable. To isolate the contribution of upper atmospheric activity, they subtracted the photospheric component from the observed NUV emission, focusing exclusively on the excess NUV flux. This excess NUV flux was then utilized to analyze the relationship between rotation and chromospheric NUV activity. Most of the stars in their sample, which had NUV detections, were slow rotators. Stelzer et al. (2016) observed two distinct regimes, a saturation regime and an unsaturated (linear) regime, in the plots of luminosity ($L'_{\rm NUV}$) versus rotation period and $L'_{\rm NUV}/L_{\rm bol}$ versus Rossby number. Here $L'_{\rm NUV}$ represents the luminosity associated with the excess NUV flux. Notably, the saturation in NUV luminosity persisted for rotation periods of up to ∼40 days, which extended beyond the critical period of ∼10 days observed in X-ray and Hα activity indicators.

Dixon et al. (2020) also used GALEX NUV data to study the rotation–activity relationship in a sample of 133 red giant stars. They found that the NUV excess is correlated with the rotation period and Rossby number, exhibiting similar trends to those found in M dwarfs. These trends include the saturation of activity among fast rotators. Likewise, Loyd et al. (2021) studied the evolution of strong UV emission lines as a function of rotation and age for early M dwarfs (M0–M2.5). They found that the surface fluxes of strong UV emission lines show saturation for rotation periods up to ∼10 days and Ro ∼ 0.1 and then a power-law decline in their values (see their Figures 4 and 5).

Similar to the work done by Stelzer et al. (2016), Dixon et al. (2020), and Loyd et al. (2021), we also attempt to investigate the excess NUV activity–rotation relationship for the sample of M dwarfs in this study. We used synthetic photospheric spectra generated using the PHOENIX atmosphere code (Allard & Hauschildt 1995; Hauschildt et al. 1999; Allard et al. 2012; Husser et al. 2013), computing a 64-layer photosphere model in radiative–convective equilibrium corresponding to the effective temperature, surface gravity, metallicity, and mass of each star. We obtained these stellar properties from the NASA Exoplanet Archive[21] and estimated metallicity using the V, J, K magnitude relation in Mann et al. (2013). These models yield fluxes consistent with that at the stellar surface, so we scaled

---

[21] https://exoplanetarchive.ipac.caltech.edu/

the values by the radius and distance (R^2/d^2). We then estimated the photospheric contribution to the NUV flux through the Swift UVM2 filter and subtracted it from the total NUV flux to estimate the excess NUV flux.

The left panel of Figure 22 compares the excess NUV luminosity of our target stars to their rotation periods, with the Stelzer et al. (2016) data points shown for context. Different symbols are used for each spectral type. Interestingly, we observe no clear trend. In contrast to the trends observed with X-ray and Hα activity indicators, it is noteworthy that some fast rotators like Wolf 359 and WX UMa exhibit relatively low levels of NUV emission, while some slow rotators like Lacaille 9352 and GJ 832 exhibit relatively high levels of NUV emission. Such a trend was also noticed by Stelzer et al. (2016). This can be attributed to the differences in the magnetic dynamo operating in those stars. While Lacaille 9352 and GJ 832 are early M dwarfs, they have solar-like dynamos. On the other hand, Wolf 359 and WX UMa are mid-M dwarfs, are fully convective, and hence have a different magnetic dynamo. The time line of the evolution of magnetic dynamos and hence activity levels is a strong function of stellar mass (West et al. 2008; Johnstone et al. 2021).

In the right panel of Figure 22, we compare the fractional NUV luminosities ($L'_{\rm NUV}/L_{\rm bol}$) to the Rossby numbers (Ro). We also overplot the results of Stelzer et al. (2016), which are represented by red circles. For each star, we estimated the values of $\tau_{\rm conv}$ based on its effective temperature ($T_{\rm eff}$) using Equation (36) from Cranmer & Saar (2011), which includes an extrapolation for $T_{\rm eff} < 3300$ K. The determination of convective turnover times for M dwarfs beyond the fully convective boundary is still a subject of debate, primarily due to the likelihood of their dynamos being driven by fundamentally different processes compared to more massive stars (Mullan & MacDonald 2001; Reiners & Basri 2007). However, Cranmer & Saar (2011) note that the extrapolation of these turnover times to lower effective temperatures aligns reasonably well with the semiempirical estimates conducted by Reiners et al. (2009). We compiled the values of Ro for two stars, Proxima Centauri and YZ Ceti, from the literature. For Proxima Centauri Ro $\sim$ 0.65 (Wright & Drake 2016), and for YZ Ceti Ro $\sim$ 0.50 (Pineda & Villadsen 2023). The values of Ro for those stars from our estimates are higher than the literature values by a factor of $\sim$2, which might be because of different theoretical models used to estimate them.

Unlike in the left panel of Figure 22, we see some trend between $L'_{\rm NUV}/L_{\rm bol}$ and Ro in the right panel. Though it is not very clear, it suggests that the saturation regime might extend beyond a value of Ro $\sim$ 0.1. This aligns with the extension of the saturation feature beyond the critical period of $\sim$10 days (for X-ray and Hα activity indicators) observed in the left panel of Figure 22 for the case of slow rotators.

5. Summary and Conclusions

We obtained an unprecedented contemporaneous Swift and TESS data set for two dozen nearby M dwarfs with supporting data from K2 and HST to examine the relationship between flare properties and activity at NUV and optical wavelengths. Our sample includes well-known nearby flaring M dwarfs such as AU Mic, Proxima Centauri, Wolf 359, YZ CMi, and Ross 614, as well as other M dwarfs with lower levels or even the absence of flare activity.

We summarize the results from this study below:

1. EV Lac, Ross 614, and YZ CMi exhibit the highest fractions of flaring time compared to the other stars in the sample. These stars flared for approximately 13% of their total observation time. Notably, these stars are young, but youth does not seem to be the only factor at play, as there are other young stars that did not flare. The average fraction of flaring time for M0–M3 dwarfs is estimated to be 2.1%, while that for M4–M6 dwarfs is 5%.
2. We do not find any discernible relationship between the rotation period and either NUV or optical flare rates.
3. We identify optical counterparts for $\sim$27% of our NUV flares. We find that almost all optical flares observed during Swift/UVOT observing windows have NUV counterparts, which suggests that the fraction of NUV flares having optical counterparts would increase if the flares were observed in NUV and optical passbands using similar cadences; the longer TESS cadences mean that some short-duration optical flares were missed.
4. NUV flares are much more frequent in comparison to optical flares. For a small sample of 15 flares sampled simultaneously at fast cadence by both TESS and Swift, we find that the NUV flare durations are similar to or longer than their optical counterparts.
5. Most of this study's M dwarf flares have energies and durations comparable to solar white-light flares. This suggests that solar flares and M dwarf flares share common scaling laws connecting reconnection timescales, released flare energies, and magnetic energies.
6. The majority (68%) of the optical flares have amplitudes less than 2% relative to quiescence, and 98% of the NUV flares had amplitudes greater than 1.5× the quiescent level. This significant difference in amplitudes of optical and NUV flares is because M dwarfs have low levels of quiescent UV fluxes, enhancing the contrast between flaring and quiescent levels.
7. We find that there is a decreasing trend in the energy fractionation ($E_{\rm TESS}/E_{\rm NUV}$) as $E_{\rm NUV}$ increases, but note that there is large scatter.
8. We present an empirical relationship between NUV ($E_{\rm NUV}$) and optical ($E_{\rm TESS}$) flare energies of the form $\log E_{\rm TESS} = 0.823 \pm 0.059 \log E_{\rm NUV} + 5.630 \pm 1.8$. Note that our optical flare energy derivation relies on the assumption of a 10,000 K BB and then conversion to TESS band energy ($E_{\rm TESS}$), due to the absence of an absolution flux calibration. Hence, others using this relationship should derive their optical flare energies in a similar fashion.
9. We evaluate the performance of various RHD models and BB models in predicting NUV flare energies from optical flare energies. We find that the RHD model, F13 +12.5*5F11, can predict the NUV flare energies from TESS flare energies more accurately than others.
10. The FFDs for both NUV and optical flares exhibit comparable slopes across all spectral types: M0–M3, M4, M5, and M6. This alignment suggests the presence of a common physical mechanism responsible for generating both UV and optical flares, as discussed in the existing literature.
11. The FFD slopes for the M0–M3, M4, and M5 dwarfs (but not the M6 dwarfs) are shallow enough that they cross into the abiogenesis zone.

Many current studies assessing the impacts of flares on exoplanets extrapolate their findings from white-light flare studies to the UV spectrum (e.g., Feinstein et al. 2020b; Howard et al. 2020). The Kepler/K2 and TESS missions have played a pivotal role in advancing the field of stellar flare science in relation to exoplanets, thanks to their high-cadence observations and extended mission durations. The relationship between NUV and optical flare properties established in this study will prove invaluable for leveraging the extensive data set of optical flares obtained by Kepler/K2 and TESS. It will enable the estimation of approximate NUV flare rates on M dwarfs, providing essential input for models aiming to predict the effects of strong flares on the atmospheres of planets orbiting flaring M dwarfs. Furthermore, understanding energy fractionation in the optical/NUV bands is crucial for exploring new aspects of flare physics and for the development of more accurate flare models.

Furthermore, the results of this paper will play a crucial role in the planning of observations of NUV flares on M dwarfs, particularly for upcoming UV missions such as the Star-Planet Activity Research CubeSat (SPARCS; Ardila et al. 2018) and the Ultraviolet Transient Astronomy Satellite (ULTRASAT; Shvartzvald et al. 2024).

Acknowledgments

We are thankful to S. Webb for helping to compile literature data of the solar and stellar flare durations obtained by various missions. This research has made use of the SVO Filter Profile Service (http://svo2.cab.inta-csic.es/theory/fps/) supported from the Spanish MINECO through grant AYA2017-84089. This work has made use of NASA's Astrophysics Data System, the SIMBAD and Vizier databases (operated at Centre de Données astronomiques de Strasbourg, Strasbourg, France). The material in this paper is based on work supported by NASA under award Nos. 80NSSC19K0104, 80NSSC19K0315, 80GSFC21M0002, 80NSSC21K0362, 80NSSC23K0155, 80NSSC21K0122, 80NSSC21K1936, and 80NSSC22K0126. We acknowledge partial funding support from GSFC Sellers Exoplanet Environments Collaboration (SEEC), which is funded by the NASA Planetary Science Division's Internal Scientist Funding Model. A portion of the presented work was also supported by NASA's Astrophysics Data Analysis Program through grant 20-ADAP20-0016. This paper includes data collected by the TESS and K2 missions, which are available from the Mikulski Archive for Space Telescopes (MAST). Data were taken from the TESS Light Curves—All Sectors archive (MAST Team 2021b), the TESS "Fast" Light Curves—All Sectors archive (MAST Team 2021a), and the K2 Light Curves Campaign 14 archive (STScI 2018). Funding for the TESS mission is provided by NASA's Science Mission directorate. This work made use of data supplied by the UK Swift Science Data Centre at the University of Leicester. This research has made use of the XRT Data Analysis Software (XRTDAS) developed under the responsibility of the ASI Science Data Center (ASDC), Italy.

This research was carried out in part at the Jet Propulsion Laboratory, California Institute of Technology, under a contract with the National Aeronautics and Space Administration (80NM0018D0004).

J.R.A.D. acknowledges support from the DiRAC Institute in the Department of Astronomy at the University of Washington. The DiRAC Institute is supported through generous gifts from the Charles and Lisa Simonyi Fund for Arts and Sciences and the Washington Research Foundation. L.D.V. acknowledges funding support from the Heising-Simons Astrophysics Postdoctoral Launch Program. This research has made use of data obtained through the High Energy Astrophysics Science Archive Research Center Online Service, provided by the NASA/Goddard Space Flight Center.

We thank the Space Telescope Science Institute for support through grant HST-GO-15463. This research is based on observations made with the NASA/ESA HST obtained from the Mikulski Archive for Space Telescopes (MAST) at the Space Telescope Science Institute, which is operated by the Association of Universities for Research in Astronomy, Inc., under NASA contract NAS 526555. The HST observations are associated with program HST-GO-15463 (PI: A. Youngblood), obtained through the Director's Discretionary Time allocation. The specific observations analyzed can be accessed via doi:10.17909/kbv1-1244.

This project was supported in part by an appointment to the NRC Research Associateship Program at the US Naval Research Laboratory in Washington, DC, administered by the Fellowships Office of the National Academies of Sciences, Engineering, and Medicine. Basic Research in Astronomy at the US Naval Research Laboratory is supported by 6.1 Base funding.

Facilities: TESS, Swift (XRT & UVOT), Kepler, HST.

Software: Astropy (Astropy Collaboration et al. 2013, 2018, 2022), Matplotlib (Hunter 2007), Numpy (Harris et al. 2020), Lightkurve (Lightkurve Collaboration et al. 2018), Python, IPython (Perez & Granger 2007), Jupyter (Kluyver et al. 2016).

Appendix A
Summary of NUV Flare Properties

A summary of NUV flare properties is given in Table 9.

Table 9
Summary of NUV Flare Properties

Name	N	N_{U}	T_{start} BJD–2457000 (days)	T_{stop} BJD–2457000 (days)	Duration (min)	Peak Flux (cnts s^{-1})	Amplitude	E_{NUV} (10^{30} erg)	log L_q (erg s^{-1})
AP Col	10	1[a]	1473.0841	1473.0869	4.2	25.4	39.1	3.8	27.4
		2	1473.2044	1473.2063	2.9	2.4	3.7	0.33	
		3[a]	1482.0536	1482.0556	3.1	10.3	14.5	1.6	
		4	1482.8307	1482.8344	5.5	8.6	9.8	1.3	
		5	1482.9663	1482.9673	1.7	4.8	5.5	0.46	
		6[a]	1484.9602	1484.9648	7.2	2.0	2.4	0.59	
		7	1485.8273	1485.8388	17.1	4.2	5.2	5.7	
		8	1485.8874	1485.8886	2.2	1.1	1.7	0.12	
		9	1485.9476	1485.9487	2.2	1.8	2.0	0.27	
		10	1486.9588	1486.9619	5.0	1.9	2.8	0.39	
			Cycle 3						
	6	11[a]	2190.0381	2190.0547	24.1	20.0	25.5	26.7	27.5
		12	2190.4401	2190.4409	1.7	1.9	2.3	0.27	
		13	2190.5027	2190.5038	1.7	3.5	3.7	0.37	
		14	2190.5099	2190.5103	1.1	2.8	2.2	0.21	
		15	2190.9098	2190.9125	4.1	3.2	3.9	1.5	
		16	2191.1105	2191.1108	0.55	2.7	2.6	0.12	
AU Mic	5	1	1340.7517	1340.7540	3.5	18.4	1.6	1.7	28.7
		2	1341.8232	1341.8249	2.8	23.5	2.2	3.5	
		3	1343.1545	1343.1556	2.2	13.0	1.5	2.4	
		4	1347.1380	1347.1421	6.1	19.7	1.6	6.8	
		5	1347.2673	1347.2767	13.6	35.5	2.9	45.5	
			Cycle 3						
	1	6[b]	2058.2364		>9.6	99.2	7.0	>96	28.8
DG CVn	3	1	1953.3826	1953.3835	1.5	11.2	6.9	3.9	28.4
		2	1953.4511	1953.4536	3.9	6.4	3.9	8.7	
		3	1953.7063	1953.7071	1.3	4.2	2.7	1.3	
DX Cnc	0								27.1

Notes. Here N is the total number of NUV flares observed on a given star in a given TESS sector, N_{U} is NUV flare ID, and T_{start} and T_{stop} are flare start and stop times, respectively, in units of BJD –2,457,000 (days). Likewise, "duration" is the total time in units of minutes during which the flare occurred and is estimated as the difference between T_{start} and T_{stop}, "Peak Flux" is the flare flux during the peak of the flare, "Amplitude" is the total height of the flare peak relative to the quiescent flux, E_{NUV} is the NUV flare energy, and L_q is the quiescent NUV luminosity of a given star. A lower limit on the flare energy is given for each of the flares that were not observed for their full duration. Optical counterpart for three NUV flares with IDs $N_{\mathrm{U}} = 16, 17, 18$ appears to be a single complex flare ($T_{\mathrm{start}} = 1483.0925$) in the TESS light curve of star Ross 614 because of longer cadence size, and hence they are not resolved as separate flares.

[a] Indicates that a given NUV flare has an optical counterpart in the TESS light curve and it was observed for full duration by Swift/UVOT.

[b] Indicates that a given NUV flare has an optical counterpart in the TESS light curve and it was not observed for full duration by Swift/UVOT.

[c] Indicates that simultaneous TESS data are not available during the flare.

(This table is available in its entirety in machine-readable form.)

Appendix B
Properties of TESS/K2 Flares That Have NUV Counterparts

Properties of TESS/K2 flares that have NUV counterparts are given in Table 10.

Table 10

Properties of TESS/K2 Flares That Have NUV Counterparts

Name	N_U	T_start BJD–2457,000 (days)	T_stop BJD–2457,000 (days)	T_peak BJD–2457,000 (days)	**ED** (s)	log E_bol (erg)	**Amplitude**
AP Col	1	1473.08486	1473.08763	1473.08486	1.8	31.1	1.008
	3	1482.05429	1482.05429	1482.05429	0.51	30.6	1.004
	6	1484.96121	1484.96538	1484.96121	1.3	31.0	1.003
	11	2190.03796	2190.05625	2190.04074	14.1	32.0	1.023
AU Mic	6	2058.2366	2058.29632	2058.2366	15.6	33.4	1.009
EV Lac	2	1748.2384	1748.2467	1748.2384	1.5	31.5	1.003
	3	1749.0273	1749.0328	1749.0286	1.2	31.3	1.003
	7	1749.2953	1749.3036	1749.2967	4.8	32.0	1.013
GJ 3631	5	2561.07581	2561.07766	2561.07581	2.0	30.9	1.02
	6	2563.2758	2563.2883	2563.2758	32.7	32.2	1.06
	7	2563.87887	2563.8791	2563.87887	0.74	30.5	1.02
	11	2568.12672	2568.12857	2568.12672	2.8	31.1	1.02
LP 776-25	1	1456.94462	1456.94601	1456.94462	0.60	31.4	1.003
	2	1461.84041	1461.84874	1461.84041	2.6	32.0	1.006
Prox. Cen.	11	1602.72307	1602.72307	1602.72307	0.16	29.5	1.001
Ross 614	1	1472.94935	1472.95213	1472.95074	0.88	30.9	1.004
	9	1479.91469	1479.91885	1479.91469	1.09	31.0	1.003
	11	1479.98413	1479.99524	1479.98413	3.0	31.4	1.006
	20	1483.90914	1483.91331	1483.90914	0.72	30.8	1.002
	21	1483.95775	1483.95914	1483.95775	0.49	30.7	1.002
V1005 Ori	1	1448.89678	1448.896787	1448.89678	0.31	31.6	1.003
Wolf 359 (TESS)	5	2567.40392	2567.40647	2567.40392	1.4	30.2	1.02
	11	2568.39059	2568.39082	2568.39059	0.25	29.5	1.007
	14	2568.98741	2569.0057	2568.98741	11.5	31.1	1.012
	19	2570.10743	2570.10789	2570.10743	0.36	29.6	1.008
	15	2570.32597	2570.32805	2570.32597	1.3	30.2	1.018
	25	2570.50654	2570.50723	2570.50654	0.43	29.7	1.008
	30	2571.11678	2571.11864	2571.11678	1.2	30.1	1.013
Wolf 359 (*K*2)	34	3075.19455	3075.19592	3075.19455	0.47	29.6	1.006
	35	3075.19728	3075.20068	3075.19728	1.12	29.95	1.004
	36	3095.656	3095.66491	3095.656	1.31	30.03	1.005
	38	3096.64361	3096.64905	3096.64361	2.25	30.26	1.0239
	41	3116.56805	3116.57895	3116.56805	0.97	29.89	1.0023
	42	3116.83094	3116.84252	3116.83094	8.05	30.81	1.0200
	44	3117.69657	3117.69861	3117.69657	0.125	29.00	1.0012
	45	3118.04322	3118.04322	3118.04322	0.06	28.695	1.0010
	46	3118.04595	3118.04799	3118.04595	0.18	29.16	1.002
	47	3118.10929	3118.11269	3118.10929	0.21	29.22	1.001
	48	3118.82235	3118.82371	3118.82235	0.36	29.46	1.003
Wolf 424	3	1949.3954	1949.3968	1949.3954	0.52	30.0	1.002
YZ CMi	2	1508.65524	1508.71219	1508.65524	122.6	33.3	1.132
	12	1513.18573	1513.19406	1513.18573	2.8	31.6	1.009
	16	1514.98985	1514.99263	1514.98985	0.81	31.1	1.003
	22	2236.9053	2236.90993	2236.9053	4.5	31.8	1.021
	24	2237.04165	2237.0435	2237.04165	0.60	31.0	1.006
	26	2237.7002	2237.70113	2237.7002	0.20	30.5	1.005
	27	2237.70622	2237.71826	2237.70622	6.26	32.0	1.013
	30	2237.78053	2237.78238	2237.78053	0.79	31.1	1.009

Note. The column N_U gives the ID of the NUV flare in Appendix A for which a given TESS/*K*2 flare in this table is its optical counterpart. The flare energies (E_bol) are the 10,000 K BB bolometric energies and can be converted to TESS band energies (E_TESS) using the ratio $E_\mathrm{TESS}/E_\mathrm{bol} = 0.18$. Similarly, the ratio of E_K2 to E_bol is 0.32 for the *K*2 band energy.

(This table is available in machine-readable form.)

ORCID iDs

Rishi R. Paudel https://orcid.org/0000-0002-8090-3570
Thomas Barclay https://orcid.org/0000-0001-7139-2724
Allison Youngblood https://orcid.org/0000-0002-1176-3391
Elisa V. Quintana https://orcid.org/0000-0003-1309-2904
Joshua E. Schlieder https://orcid.org/0000-0001-5347-7062
Laura D. Vega https://orcid.org/0000-0002-5928-2685
Emily A. Gilbert https://orcid.org/0000-0002-0388-8004
Rachel A. Osten https://orcid.org/0000-0001-5643-8421
Sarah Peacock https://orcid.org/0000-0002-1046-025X
Isaiah I. Tristan https://orcid.org/0000-0001-5974-4758
Dax L. Feliz https://orcid.org/0000-0002-2457-7889
Patricia T. Boyd https://orcid.org/0000-0003-0442-4284
James R. A. Davenport https://orcid.org/0000-0002-0637-835X
Daniel Huber https://orcid.org/0000-0001-8832-4488
Adam F. Kowalski https://orcid.org/0000-0001-7458-1176
Teresa Monsue https://orcid.org/0000-0003-3896-3059
Michele L. Silverstein https://orcid.org/0000-0003-2565-7909

References

Allard, F., & Hauschildt, P. H. 1995, ApJ, 445, 433
Allard, F., Homeier, D., & Freytag, B. 2012, RSPTA, 370, 2765
Allred, J. C., Kowalski, A. F., & Carlsson, M. 2015, ApJ, 809, 104
Andreoni, I., & Cooke, J. 2019, in IAU Symp. 339, Southern Horizons in Time-Domain Astronomy, 135
Anglada-Escudé, G., Amado, P. J., Barnes, J., et al. 2016, Natur, 536, 437
Anglada-Escude, G., Arriagada, P., Tuomi, M., et al. 2014, MNRAS, 443, L89
Ardila, D. R., Shkolnik, E., Scowen, P., et al. 2018, arXiv:1808.09954
Astropy Collaboration, Price-Whelan, A. M., Lim, P. L., et al. 2022, ApJ, 935, 167
Astropy Collaboration, Price-Whelan, A. M., Sipőcz, B. M., et al. 2018, AJ, 156, 123
Astropy Collaboration, Robitaille, T. P., Tollerud, E. J., et al. 2013, A&A, 558, A33
Astudillo-Defru, N., Delfosse, X., Bonfils, X., et al. 2017a, A&A, 600, A13
Astudillo-Defru, N., Díaz, R. F., Bonfils, X., et al. 2017b, A&A, 605, L11
Bailer-Jones, C. A. L., Rybizki, J., Fouesneau, M., Demleitner, M., & Andrae, R. 2021, AJ, 161, 147
Baroch, D., Morales, J. C., Ribas, I., et al. 2020, A&A, 641, A69
Bartlett, J. L., Lurie, J. C., Riedel, A., et al. 2017, AJ, 154, 151
Bell, C. P. M., Mamajek, E. E., & Naylor, T. 2015, MNRAS, 454, 593
Benz, W., Broeg, C., Fortier, A., et al. 2021, ExA, 51, 109
Berger, V. L., Hinkle, J. T., Tucker, M. A., et al. 2023, arXiv:2312.12511
Bonnefoy, M., Chauvin, G., Lagrange, A. M., et al. 2014, A&A, 562, A127
Bortle, A., Fausey, H., Ji, J., et al. 2021, AJ, 161, 230
Borucki, W. J., Koch, D., Basri, G., et al. 2010, Sci, 327, 977
Bowens-Rubin, R., Akana Murphy, J. M., Hinz, P. M., et al. 2023, AJ, 166, 260
Boyajian, T. S., von Braun, K., van Belle, G., et al. 2012, ApJ, 757, 112
Brasseur, C. E., Osten, R. A., & Fleming, S. W. 2019, ApJ, 883, 88
Brasseur, C. E., Osten, R. A., Tristan, I. I., & Kowalski, A. F. 2023, ApJ, 944, 5
Bryden, G., Beichman, C. A., Carpenter, J. M., et al. 2009, ApJ, 705, 1226
Burrows, D. N., Hill, J. E., Nousek, J. A., et al. 2005, SSRv, 120, 165
Cardona Guillén, C., Lodieu, N., Béjar, V. J. S., et al. 2021, A&A, 654, A134
Carlsson, M., & Stein, R. F. 1992, ApJL, 397, L59
Carlsson, M., & Stein, R. F. 1995, ApJL, 440, L29
Carlsson, M., & Stein, R. F. 1997, ApJ, 481, 500
Chavali, S., Youngblood, A., Paudel, R. R., et al. 2022, RNAAS, 6, 201
Cifuentes, C., Caballero, J. A., Cortés-Contreras, M., et al. 2020, A&A, 642, A115
Collins, J. M., Jones, H. R. A., & Barnes, J. R. 2017, A&A, 602, A48
Correia, A. C. M., Couetdic, J., Laskar, J., et al. 2010, A&A, 511, A21
Cranmer, S. R., & Saar, S. H. 2011, ApJ, 741, 54
Davenport, J. R. A. 2016, ApJ, 829, 23
Debes, J. H., Jang-Condell, H., Weinberger, A. J., Roberge, A., & Schneider, G. 2013, ApJ, 771, 45
Dixon, D., Tayar, J., & Stassun, K. G. 2020, AJ, 160, 12
Donati, J. F., Morin, J., Petit, P., et al. 2008, MNRAS, 390, 545
Douglas, S. T., Agüeros, M. A., Covey, K. R., et al. 2014, ApJ, 795, 161
Dreizler, S., Jeffers, S. V., Rodríguez, E., et al. 2020, MNRAS, 493, 536
Dressing, C. D., & Charbonneau, D. 2015, ApJ, 807, 45
Engle, S. G., & Guinan, E. F. 2017, ATel, 10678
Engle, S. G., & Guinan, E. F. 2023a, ApJL, 954, L50
Engle, S. G., & Guinan, E. F. 2023b, ApJL, 954, L50
Feinstein, A., Montet, B., & Ansdell, M. 2020a, JOSS, 5, 2347
Feinstein, A. D., Montet, B. T., Ansdell, M., et al. 2020b, AJ, 160, 219
Foreman-Mackey, D., Agol, E., Angus, R., et al. 2017, dfm/celerite: celerite v0.2.1, v0.2.1, Zenodo, doi:10.5281/zenodo.806847
Foreman-Mackey, D., Hogg, D. W., Lang, D., & Goodman, J. 2013, PASP, 125, 306
France, K., Duvvuri, G., Egan, H., et al. 2020, AJ, 160, 237
Fuhrmeister, B., Liefke, C., Schmitt, J. H. M. M., & Reiners, A. 2008, A&A, 487, 293
Gagné, J., Lafrenière, D., Doyon, R., Malo, L., & Artigau, É. 2014, ApJ, 783, 121
Gaidos, E., Mann, A. W., Lépine, S., et al. 2014, MNRAS, 443, 2561
Gáspár, A., Rieke, G. H., & Balog, Z. 2013, ApJ, 768, 25
Gershberg, R. E. 1972, Ap&SS, 19, 75
Gershberg, R. E. 2005, Solar-Type Activity in Main-Sequence Stars (Berlin: Springer)
Gilbert, E. A., Barclay, T., Quintana, E. V., et al. 2022, AJ, 163, 147
Gilliland, R. L., Jenkins, J. M., Borucki, W. J., et al. 2010, ApJL, 713, L160
Gizis, J. E. 1997, AJ, 113, 806
Guinan, E. F., Engle, S. G., & Durbin, A. 2016, ApJ, 821, 81
Günther, M. N., Zhan, Z., Seager, S., et al. 2020, AJ, 159, 60
Hardegree-Ullman, K. K., Cushing, M. C., Muirhead, P. S., & Christiansen, J. L. 2019, AJ, 158, 75
Harris, C. R., Millman, K. J., van der Walt, S. J., et al. 2020, Natur, 585, 357
Hauschildt, P. H., Allard, F., & Baron, E. 1999, ApJ, 512, 377
Hawley, S. L., & Fisher, G. H. 1992, ApJS, 78, 565
Hawley, S. L., Gizis, J. E., & Reid, I. N. 1996, AJ, 112, 2799
Hawley, S. L., & Pettersen, B. R. 1991, ApJ, 378, 725
Henry, T. J., Jao, W.-C., Subasavage, J. P., et al. 2006, AJ, 132, 2360
Henry, T. J., Walkowicz, L. M., Barto, T. C., & Golimowski, D. A. 2002, AJ, 123, 2002
Hogg, D. W., Bovy, J., & Lang, D. 2010, arXiv:1008.4686
Houdebine, E. ´, Mullan, D. J., Doyle, J. G., et al. 2019, AJ, 158, 56
Houdebine, E. R., Mullan, D. J., Paletou, F., & Gebran, M. 2016, ApJ, 822, 97
Howard, W. S., Corbett, H., Law, N. M., et al. 2020, ApJ, 902, 115
Howard, W. S., & MacGregor, M. A. 2022, ApJ, 926, 204
Howell, S. B., Sobeck, C., Haas, M., et al. 2014, PASP, 126, 398
Hunter, J. D. 2007, CSE, 9, 90
Husser, T. O., Wende-von Berg, S., Dreizler, S., et al. 2013, A&A, 553, A6
Jackman, J. A. G., Shkolnik, E. L., Million, C., et al. 2023, MNRAS, 519, 3564
Jeffers, S. V., Dreizler, S., Barnes, J. R., et al. 2020, Sci, 368, 1477
Jeffers, S. V., Schöfer, P., Lamert, A., et al. 2018, A&A, 614, A76
Jenkins, J. M., Caldwell, D. A., Chandrasekaran, H., et al. 2010, ApJL, 713, L120
Jenkins, J. M., Twicken, J. D., McCauliff, S., et al. 2016, Proc. SPIE, 9913, 99133E
Johnstone, C. P., Bartel, M., & Güdel, M. 2021, A&A, 649, A96
Joy, A. H., & Abt, H. A. 1974, ApJS, 28, 1
Kawai, H., Tsuboi, Y., Iwakiri, W. B., et al. 2022, PASJ, 74, 477
Kervella, P., Mérand, A., Ledoux, C., Demory, B. O., & Le Bouquin, J. B. 2016, A&A, 593, A127
Kervella, P., Thévenin, F., Ségransan, D., et al. 2003, A&A, 404, 1087
Kirkpatrick, J. D., Henry, T. J., & McCarthy, D. W. J. 1991, ApJS, 77, 417
Kluyver, T., Ragan-Kelley, B., Pérez, F., et al. 2016, in Positioning and Power in Academic Publishing: Players, Agents and Agendas, ed. F. Loizides & B. Schmidt (Amsterdam: IOS Press), 87
Kowalski, A. F. 2022, FrASS, 9, 351
Kowalski, A. F., Allred, J. C., Uitenbroek, H., et al. 2017, ApJ, 837, 125
Kowalski, A. F., Hawley, S. L., Wisniewski, J. P., et al. 2013, ApJS, 207, 15
Kowalski, A. F., Mathioudakis, M., Hawley, S. L., et al. 2016, ApJ, 820, 95
Kowalski, A. F., Wisniewski, J. P., Hawley, S. L., et al. 2019, ApJ, 871, 167
Lacy, C. H., Moffett, T. J., & Evans, D. S. 1976, ApJS, 30, 85
Lightkurve Collaboration, Cardoso, J. V. D. M., Hedges, C., et al., 2018 Lightkurve: Kepler and TESS Time Series Analysis in Python, Astrophysics Source Code Library, ascl:1812.013
Lin, C.-L., Chen, W.-P., Ip, W.-H., et al. 2021, AJ, 162, 11

López-Valdivia, R., Mace, G. N., Sokal, K. R., et al. 2019, ApJ, 879, 105
Loyd, R. O. P., France, K., Youngblood, A., et al. 2018, ApJ, 867, 71
Loyd, R. O. P., Shkolnik, E. L., Schneider, A. C., et al. 2021, ApJ, 907, 91
MacDonald, J., Mullan, D. J., & Dieterich, S. 2018, ApJ, 860, 15
Maehara, H., Notsu, Y., Namekata, K., et al. 2021, PASJ, 73, 44
Maehara, H., Shibayama, T., Notsu, Y., et al. 2015, EP&S, 67, 59
Mamajek, E. E. 2012, ApJL, 754, L20
Mamajek, E. E., Bartlett, J. L., Seifahrt, A., et al. 2013, AJ, 146, 154
Mamajek, E. E., & Bell, C. P. M. 2014, MNRAS, 445, 2169
Mann, A. W., Brewer, J. M., Gaidos, E., Lépine, S., & Hilton, E. J. 2013, AJ, 145, 52
Mann, A. W., Feiden, G. A., Gaidos, E., Boyajian, T., & von Braun, K. 2015, ApJ, 804, 64
Martin, C. D., Bianchi, L., Donas, J., et al. 1999, in ASP Conf. Ser. 164, Ultraviolet-Optical Space Astronomy Beyond HST, ed. J. A. Morse, J. M. Shull, & A. L. Kinney, 182
MAST Team 2021a, TESS "Fast" Light Curves — All Sectors, STScI/MAST
MAST Team 2021b, TESS Light Curves — All Sectors, STScI/MAST
Micela, G., Pye, J., & Sciortino, S. 1997, A&A, 320, 865
Micela, G., Sciortino, S., Serio, S., et al. 1985, ApJ, 292, 172
Mighell, K. J., & Plavchan, P. 2013, AJ, 145, 148
Mohanty, S., & Basri, G. 2003, ApJ, 583, 451
Mullan, D. J., & MacDonald, J. 2001, ApJ, 559, 353
Namekata, K., Sakaue, T., Watanabe, K., et al. 2017, ApJ, 851, 91
Newton, E. R., Charbonneau, D., Irwin, J., & Mann, A. W. 2015, ApJ, 800, 85
Newton, E. R., Irwin, J., Charbonneau, D., et al. 2017, ApJ, 834, 85
Noyes, R. W., Hartmann, L. W., Baliunas, S. L., Duncan, D. K., & Vaughan, A. H. 1984, ApJ, 279, 763
Osten, R. A., Hawley, S. L., Allred, J. C., Johns-Krull, C. M., & Roark, C. 2005, ApJ, 621, 398
Osten, R. A., Kowalski, A., Drake, S. A., et al. 2016, ApJ, 832, 174
Paegert, M., Stassun, K. G., Collins, K. A., et al. 2021, arXiv:2108.04778
Paudel, R. R., Barclay, T., Schlieder, J. E., et al. 2021, ApJ, 922, 31
Paudel, R. R., Gizis, J. E., Mullan, D. J., et al. 2018a, ApJ, 858, 55
Paudel, R. R., Gizis, J. E., Mullan, D. J., et al. 2018b, ApJ, 861, 76
Paudel, R. R., Gizis, J. E., Mullan, D. J., et al. 2020, MNRAS, 494, 5751
Perez, F., & Granger, B. E. 2007, CSE, 9, 21
Pineda, J. S., & Villadsen, J. 2023, NatAs, 7, 569
Pineda, J. S., Youngblood, A., & France, K. 2021, ApJ, 911, 111
Pizzolato, N., Maggio, A., Micela, G., Sciortino, S., & Ventura, P. 2003, A&A, 397, 147
Plavchan, P., Barclay, T., Gagné, J., et al. 2020, Natur, 582, 497
Pozuelos, F. J., Suárez, J. C., de Elía, G. C., et al. 2020, A&A, 641, A23
Rajpurohit, A. S., Allard, F., Rajpurohit, S., et al. 2018, A&A, 620, A180
Ranjan, S., Schwieterman, E. W., Harman, C., et al. 2020, ApJ, 896, 148
Reiners, A., & Basri, G. 2007, ApJ, 656, 1121
Reiners, A., Basri, G., & Browning, M. 2009, ApJ, 692, 538
Rekhi, P., Ben-Ami, S., Perdelwitz, V., & Shvartzvald, Y. 2023, ApJ, 955, 24
Ricker, G. R., Winn, J. N., Vanderspek, R., et al. 2015, JATIS, 1, 014003
Riedel, A. R., Finch, C. T., Henry, T. J., et al. 2014, AJ, 147, 85
Riedel, A. R., Murphy, S. J., Henry, T. J., et al. 2011, AJ, 142, 104
Rimmer, P. B., Xu, J., Thompson, S. J., et al. 2018, SciA, 4, eaar3302
Roming, P. W. A., Kennedy, T. E., Mason, K. O., et al. 2005, SSRv, 120, 95
Rugheimer, S., Kaltenegger, L., Segura, A., Linsky, J., & Mohanty, S. 2015a, ApJ, 809, 57
Rugheimer, S., Segura, A., Kaltenegger, L., & Sasselov, D. 2015b, ApJ, 806, 137
Schlieder, J. E., Lépine, S., & Simon, M. 2012, AJ, 143, 80
Schmidt, S. J., Prieto, J. L., Stanek, K. Z., et al. 2014, ApJL, 781, L24
Schmitt, J. H. M. M., Ioannidis, P., Robrade, J., Czesla, S., & Schneider, P. C. 2019, A&A, 628, A79
Sebastian, D., Gillon, M., Ducrot, E., et al. 2021, A&A, 645, A100
Shibayama, T., Maehara, H., Notsu, S., et al. 2013, ApJS, 209, 5
Shulyak, D., Reiners, A., Engeln, A., et al. 2017, NatAs, 1, 0184
Shvartzvald, Y., Waxman, E., Gal-Yam, A., et al. 2024, ApJ, 964, 74
Sirianni, M., Jee, M. J., Benítez, N., et al. 2005, PASP, 117, 1049
Solanki, S. K. 2009, in ASP Conf. Ser. 405, Solar Polarization 5: In Honor of Jan Stenflo, ed. S. V. Berdyugina, K. N. Nagendra, & R. Ramelli, 135
Stassun, K. G., Oelkers, R. J., Paegert, M., et al. 2019, AJ, 158, 138
Stelzer, B., Damasso, M., Scholz, A., & Matt, S. P. 2016, MNRAS, 463, 1844
Stelzer, B., Marino, A., Micela, G., López-Santiago, J., & Liefke, C. 2013, MNRAS, 431, 2063
STScI 2018, K2 Light Curves Campaign 14, STScI/MAST, doi:10.17909/T9BC75
Suárez Mascareño, A., Rebolo, R., González Hernández, J. I., & Esposito, M. 2015, MNRAS, 452, 2745
Torres, C. A. O., Quast, G. R., da Silva, L., et al. 2006, A&A, 460, 695
Tristan, I. I., Notsu, Y., Kowalski, A. F., et al. 2023, ApJ, 951, 33
Veyette, M. J., & Muirhead, P. S. 2018, ApJ, 863, 166
Vilhu, O. 1984, A&A, 133, 117
Webb, S., Flynn, C., Cooke, J., et al. 2021, MNRAS, 506, 2089
West, A. A., Hawley, S. L., Bochanski, J. J., et al. 2008, AJ, 135, 785
Wright, N. J., & Drake, J. J. 2016, Natur, 535, 526
Wright, N. J., Drake, J. J., Mamajek, E. E., & Henry, G. W. 2011, ApJ, 743, 48
Zuckerman, B. 2019, ApJ, 870, 27